Elevated levels of OH observed in haze events during wintertime in central Beijing

Eloise J. Slater[1], Lisa K. Whalley[1,2], Robert Woodward-Massey[1,a], Chunxiang Ye[1,a], James D Lee[3,4], Freya Squires[4], James R. Hopkins[3,4], Rachel E Dunmore[4], Marvin Shaw[3,4], Jacqueline F. Hamilton[4], Alastair C Lewis[3,4], Leigh R. Crilley[5,b], Louisa Kramer[5], William Bloss[5], Tuan Vu[5], Yele Sun[6], Weiqi Xu[6], Siyao Yue[6], Lujie Ren[6], W. Joe F. Acton[7], C. Nicholas Hewitt[7], Xinming Wang[8], Pingqing Fu[9] and Dwayne E. Heard[1]

[1]School of Chemistry, University of Leeds, Leeds, LS2 9JT, UK

[2]National Centre for Atmospheric Science, University of Leeds, Leeds, LS2 9JT, UK

[3]National Centre for Atmospheric Science, University of York, Heslington, York, YO10 5DD, UK

[4]Wolfson Atmospheric Chemistry Laboratories, Department of Chemistry, University of York, Heslington, York, YO10 5DD, UK

[5]School of Geography, Earth and Environmental Sciences, University of Birmingham, B15 2TT, Birmingham, UK

[6]State Key Laboratory of Atmospheric Boundary Layer Physics and Atmospheric Chemistry, Institute for Atmospheric Physics, Chinese Academy of Sciences, 40 Huayanli, Chaoyang District, Beijing 100029, China

[7]Lancaster Environment Centre, Lancaster University, Lancaster, LA1 4YW, UK

[8]State Key Laboratory of Organic Geochemistry, Guangzhou Institute of Geochemistry, Chinese Academy of Sciences, 511 Kehua Street, Wushan, Tianhe District, Guangzhou, GD 510640 , China

[9] Institute of Surface-Earth System Science, Tianjin University, Tianjin 300072, China

[a]Now at: College of Environmental Sciences and Engineering, Peking University, Beijing, 100871, China

[b]Now at Department of Chemistry, Faculty of Science, York University, 4700 Keele Street, Toronto ON, M3J 1P3, Canada

Correspondence to: Dwayne Heard (d.e.heard@leeds.ac.uk) and Lisa Whalley (l.k.whalley@leeds.ac.uk)

Abstract

Wintertime *in situ* measurements of OH, HO_2 and RO_2 radicals and OH reactivity were made in central Beijing during November and December 2016. Exceptionally elevated NO was observed on occasions, up to ~250 ppbv. The daily maximum mixing ratios for radical species varied significantly day-to-day over the range 1 - 8 x 10^6 cm^{-3} (OH), 0.2 - 1.5 x 10^8 cm^{-3} (HO_2) and 0.3 - 2.5 x 10^8 cm^{-3} (RO_2). Averaged over the full observation period, the mean daytime peak in radicals was 2.7 x 10^6 cm^{-3}, 0.39 x 10^8 cm^{-3} and 0.88 x 10^8 cm^{-3} for OH, HO_2 and total RO_2, respectively. The main daytime source of new radicals *via* initiation processes (primary production) was the photolysis of HONO (~83 %), and the dominant termination pathways were the reactions of OH with NO and NO_2, particularly under polluted, haze conditions. The Master Chemical Mechanism (MCM) v3.3.1 operating within a box model was used to simulate the concentrations of OH, HO_2 and RO_2. The model underpredicted OH, HO_2 and RO_2, especially when NO mixing ratios were high (above 6 ppbv). The observation-to-model ratio of OH, HO_2 and RO_2 increased from ~ 1 (for all radicals) at 3 ppbv of NO to a factor of ~3, ~20 and ~91 for OH, HO_2 and RO_2, respectively, at ~200 ppbv of NO. The significant underprediction of radical concentrations by the MCM suggests a deficiency in the representation of gas-phase chemistry at high NO_x. The OH concentrations were surprisingly similar (within 20 % during the day) inside and outside

of haze events, despite $j(O^1D)$ decreasing by 50% during haze periods. These observations provide strong evidence that gas-phase oxidation by OH can continue to generate secondary pollutants even under high pollution episodes, despite the reduction in photolysis rates within haze.

1. Introduction

In China, especially its capital city, Beijing, air pollution and air quality are serious concerns (Tang et al., 2017). Beijing can experience severe haze episodes (Hu et al., 2014; Lang et al., 2017) with high particulate matter loadings during winter months, and high ozone episodes during the summer (Cheng et al., 2016; Wang et al., 2015). China has one of the world's fastest expanding economies and has rapidly increased its urban population to form numerous megacities. From 1980 to 2005, the fraction of the population living in urban areas of China increased from 20 to 40 %. China's economic growth has led to an increase in energy consumption, with 50% of the global demand for coal accounted for by China in 2016 (Qi et al., 2016). The Chinese government have been implementing air quality controls in China (Zhang et al., 2016a) and emission and concentrations of primary pollutants have been decreasing nationwide, however, secondary pollutants still remain a major concern (Huang et al., 2014).

The OH radical mediates virtually all oxidative chemistry during the daytime, and converts primary pollutants into secondary pollutants, as shown in Figure 1. The reaction of OH with primary pollutant emissions (particularly NO_x ($NO+NO_2$), SO_2 and VOCs (volatile organic carbon)) can form secondary pollutants such as HNO_3, H_2SO_4 and secondary oxygenated organic compounds (OVOCs). These secondary pollutants can lead to the formation of secondary aerosol and contribute to the mass of $PM_{2.5}$. During the photochemical cycle initiated by OH, NO can be oxidised to form NO_2 via reaction with HO_2 and organic peroxy radicals, RO_2, and the subsequent photolysis of NO_2 can lead to the net formation of ozone. It has been shown in previous field campaigns that measured mixing ratios of radicals have a strong dependence with $j(O^1D)$ (Ehhalt and Rohrer, 2000; Ma et al., 2019; Stone et al., 2012; Tan et al., 2018). Hence, the radical concentrations measured during wintertime are typically expected to be lower than in the summertime due to lower photolysis rates of primary radical sources such as O_3, HONO and HCHO. Here we define primary production as any process which initiates the formation of radicals and hence the photochemical chain reaction. Also, the lower temperatures experienced in the winter lead to lower water vapour concentrations and this is expected to further limit primary OH formation via $(O^1D) + H_2O$ (Heard and Pilling, 2003).

In contrast to the expectation of limited photochemistry in winter, particularly during haze episodes when light levels are reduced, aerosol composition analysis has highlighted that the contribution of secondary aerosol to the total particulate mass increases during pollution events in the North China

Plain (NCP) (Huang et al., 2014), suggesting that chemical oxidation still plays an important role in aerosol formation in winter. To fully understand the role of the OH radical during haze events experienced in central Beijing, direct *in situ* measurements of ambient OH concentration are required.
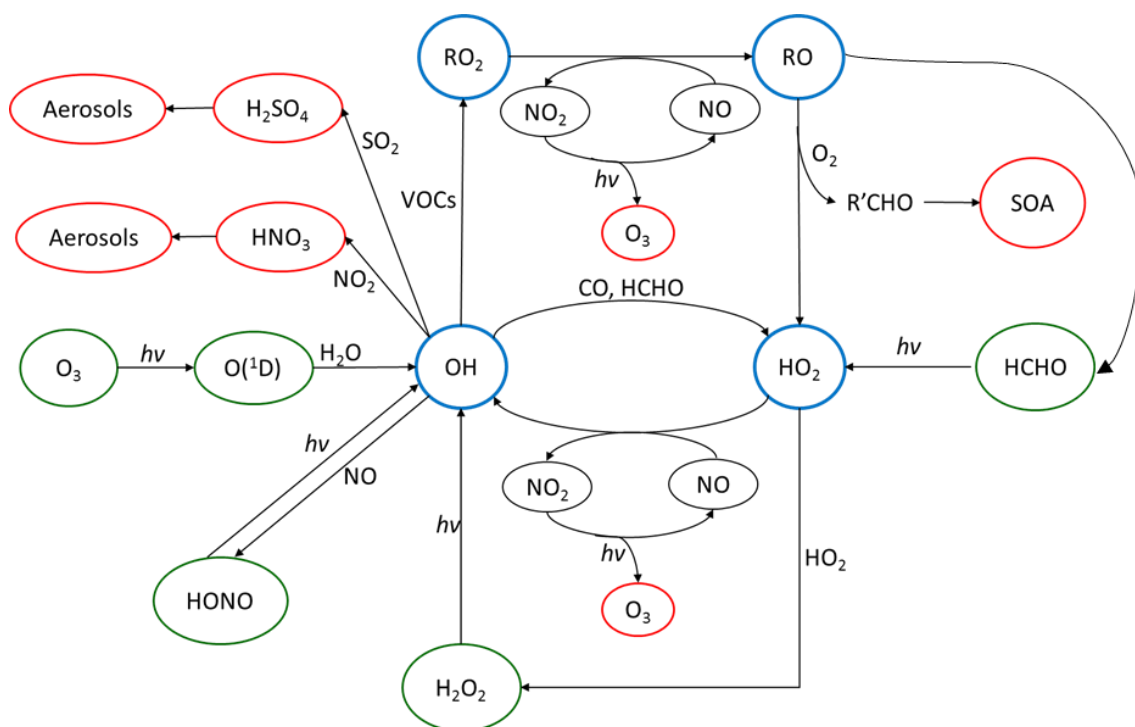

Figure 1. The tropospheric photochemical cycle, with the green circles representing species acting as routes for radical formation, the blue circles representing the radical species themselves and the red circles representing the formation of secondary pollutants. The cycle does not show any heterogeneous source (e.g. heterogeneous production of HONO) or loss processes for the radical species. It should be noted the measured HONO abundance cannot be explained by the reaction of OH + NO alone.

Measurements of OH and HO_2 in northern China during the wintertime have only recently been made. The first measurements were made during the BEST-ONE campaign (Tan et al., 2017) that took place in January 2016 in Huairou, which is a suburban site 60 km northeast from Beijing. The average daytime maximum concentrations observed during the BEST-ONE campaign for OH, HO_2 and RO_2 were 2.5×10^6 cm^{-3}, 0.8×10^8 cm^{-3} (3.2 pptv) and 0.6×10^8 cm^{-3} (2.4 pptv) respectively. The concentration of OH during the BEST-ONE campaign was an order of magnitude higher than predicted by global models over the North China Plain region (Lelieveld et al., 2016), and is consistent with the increase in secondary aerosol contribution to $PM_{2.5}$ observed during haze events (Huang et al., 2014). The radical measurements during the BEST-ONE campaign were separated into clean and polluted periods (OH reactivity (k_{OH}) > 15 s^{-1}) with an average daily maximum OH concentration for these periods of 4×10^6 cm^{-3} and 2.3×10^6 cm^{-3}, respectively. The RACM2-LIM1 (Regional Atmospheric Chemistry Model coupled with Leuven Isoprene Mechanism 1) box model was used to simulate the radical

concentrations measured during BEST-ONE (Tan et al., 2018) but these could not reproduce the OH concentration observed when NO was above 1 ppbv or below 0.6 ppbv; consistent with previous campaigns when OH was measured and modelled under NO concentrations > 1 ppbv (Emmerson et al., 2005; Kanaya et al., 2007; Lu et al., 2013; Tan et al., 2017; Zhou et al., 2003). More recently, OH and HO_2 were measured in central Beijing during winter-time at the Peking University (PKU) campus in November/December 2017 (Ma et al., 2019). The radical measurements were simulated using the RACM2-LIM1 box model which highlighted an under-prediction of the OH concentration when NO exceeded 1 ppbv (Ma et al., 2019). Two further campaigns have taken place in northern China during the summertime. The first took place in 2006 at a suburban site in Yufa (Lu et al., 2013), which is 40 km south of Beijing. The second took place in 2014 at the rural site in Wangdu (Tan et al., 2017). In both the Wangdu and Yufa field campaigns, the box model calculations underestimated the OH concentration when NO was below 0.5 ppbv. When NO exceeded 2 ppbv, a missing peroxy radical source was found, leading to a large underestimation of local ozone production by the model.

To try to understand the link between radical chemistry and the extremely high air pollution that is seen during Beijing in the wintertime, a field campaign "Air Pollution and Human Health in Chinese Megacities" (APHH) took place in central Beijing from November to December in 2016. Simultaneous measurements of OH, HO_2, and RO_2 concentrations were performed during the APHH campaign. OH reactivity (k(OH)), which is the sum of the concentration of species (X_i) that react with OH multiplied by the corresponding bimolecular rate coefficient, k_{OH+Xi}, along with other trace gas and aerosol measurements were made alongside the radicals.

In this paper we present the measurements of OH, HO_2, RO_2 and OH reactivity from the winter campaign. The concentrations of the radical species are compared to model results from the Master Chemical Mechanism (MCM3.3.1.) to assess if the radical concentrations can be simulated across the range of measured NO_x, with a particular focus under on the high NO_x conditions that were experienced. The importance of OH-initiated oxidation processes on the formation of ozone and SOA in the wintertime in Beijing are demonstrated.

2 Experimental

2.1 Location of the field measurement site

The observations took place in central Beijing at the Institute of Atmospheric Physics (IAP), which is part of the Chinese Academy of Sciences; the location of the site is shown in Figure 2, and is ~ 6.5 km from the Forbidden City. Beijing is the capital city of China and is located on the northwest border of the North China Plain (NCP). It is surrounded by the Yanshan Mountains in the west, north and northeast (Chan and Yao, 2008). The topography of Beijing allows for the accumulation of pollutants,

especially when southerly winds carrying emissions from the industrial regions are experienced. As shown by Figure 2, the measurement site was within 100m of a major road, thus local anthropogenic emissions likely influence the site, although no rush hour was observed from the diel variation of the trace gas measurements (see Figure 5). The site was also close to local restaurants and a petrol station. More details of the measurement site and instrumentation can be found in the APHH overview paper (Shi et al., 2018). The instruments were housed in containers and located on the ground at the IAP site on a grassed area, the distance between the Leeds and York container (VOC and trace gas measurements) was ~3 m.
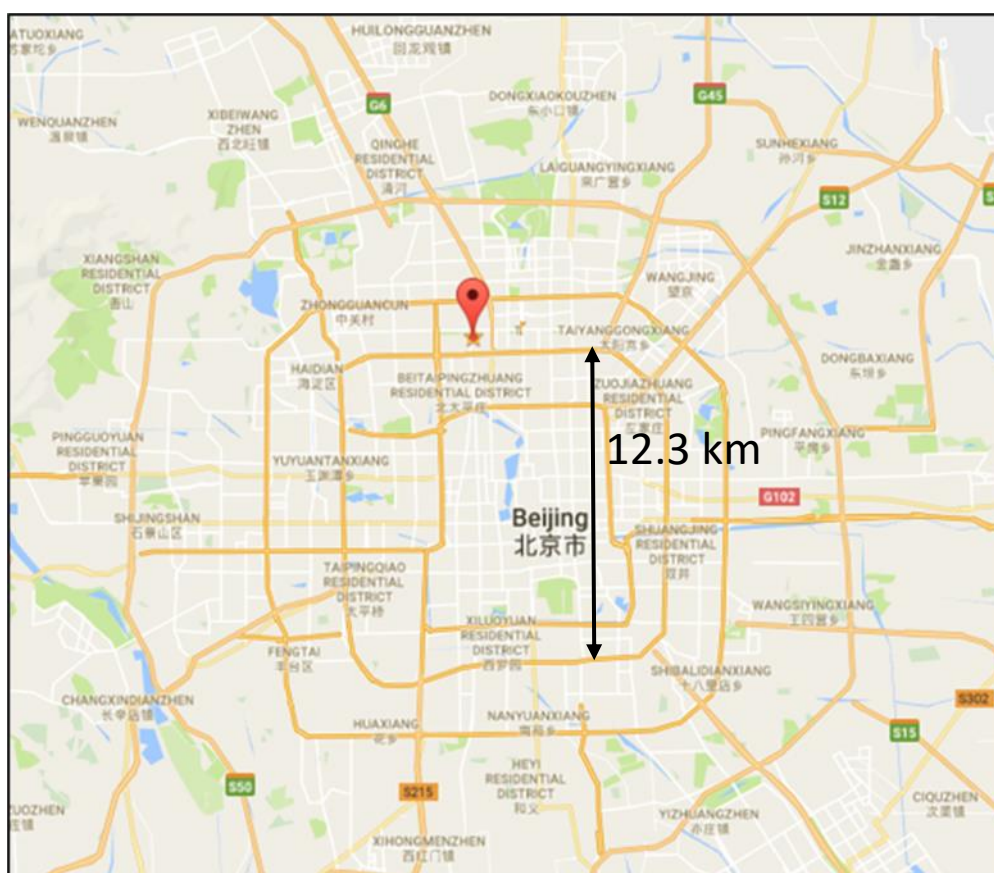

Figure 2. Location of the Institute of Atmospheric Physics, Chinese Academy of Sciences (source: ©Google Maps), the location (39°58'33'' N, 116°22'41'' E) of the APHH campaign.

2.2 Instrumental details

2.2.1 OH, HO$_2$ and RO$_2$ measurements

The University of Leeds ground-based FAGE (fluorescence assay by gas expansion) instrument (Whalley et al., 2010) was deployed at the IAP site and made measurements of OH, HO$_2$ and RO$_2$ radicals, as well as OH reactivity (k(OH)). A general outline, specific set-up and the running conditions during APHH are described here. Further details on the methodology for sequential measurements of OH and HO$_2$ that are made in the first fluorescence cell (HO$_x$) and sequential measurements of HO$_2$*

and RO_2 using the RO_xLIF method (described in detail below) in the second cell (RO_x) can be found in Whalley et al. (2018). HO_2^* refers to the measurement of HO_2 and complex RO_2 species; complex RO_2 are RO_2 species that are formed from alkene and aromatic VOCs, or VOCs that have a carbon chain greater than C_4 and which under certain conditions are detected together with HO_2 (Whalley et al., 2018). The radical measurements were made from a 6.1 m air-conditioned shipping container which has been converted into a mobile laboratory. The FAGE instrument has two detection cells which are located on top of the shipping container (sampling height of 3.5 metres) within a weather-proof housing. A Nd:YAG pumped Ti:Sapphire laser (Photonics Industries) generated pulsed tuneable near IR radiation at a pulse repetition rate of 5 kHz, which was frequency doubled then tripled using two non-linear crystals to produce UV light at 308 nm and used to excite OH via the $Q_1(1)$ transition of the $A^2\Sigma^+$, v'=0 $\leftarrow$ $X^2\Pi_i$, v''=0 band.

During the APHH campaign the configuration of the two detection cells was the same as deployed during the ClearfLo campaign in London (Whalley et al., 2018), with the two cells coupled together via a connecting side arm, which enabled the laser light exiting the HO_x cell to pass directly into the RO_x cell. The channel photo-multiplier (CPM) detectors that were used to detect fluorescence previously (Whalley et al., 2018) have been replaced by gated MCPs (micro-channel plates, Photek PMT325/Q/BI/G) and fast gating units, Photek GM10-50B) for the APHH project.

The ROxLIF flow reactor (83 cm in length, 6.4 cm in diameter) was coupled to the second FAGE detection cell to allow for detection of RO_2 (total, complex and simple) using the method outlined by Fuchs et al. (2008). The flow reactor was held at ~30 Torr and drew ~7.5 SLM through a 1 mm pinhole ID (in-diameter). The flow reactor was operated in two mode: in the first (HO_x mode) 125 sccm of CO (Messer, 10% in N_2) was mixed with ambient air close to the pinhole to convert OH to HO_2. In the second (RO_x mode), 25 sccm of NO in N_2 (Messer, 500 ppmv) was also added to the CO flow to convert RO_2 into OH. The CO present during RO_x mode rapidly converts the OH formed into HO_2. The air from the ROxLIF flow reactor was drawn (5 SLM) into the FAGE fluorescence cell (held at ~1.5 Torr) and NO (Messer, 99.9%) was injected into the fluorescence cell to convert HO_2 to OH. In HO_x mode a measure of OH + HO_2 + cRO_2 (complex RO_2) was obtained; whilst RO_x measured OH + HO_2 + ΣRO_2. sRO_2 (simple RO_2) concentration was determined by subtracting the concentration of cRO_2, HO_2 and OH from RO_x.

In previous laboratory experiments the sensitivity of the instrument to a range of different RO_2 was investigated and can be found in Whalley et al.(2018). Similar sensitivities were determined for a range of RO_2 species that were tested and agreed well with model-determined sensitivities. For comparison of the modelled RO_2 to the observed RO_2-total, RO_2-complex and RO_2-simple, the ROxLIF instrument sensitivity towards each RO_2 species in the model was determined by running a model first under the

180   RO$_x$LIF reactor and then the RO$_x$LIF FAGE cell conditions (NO concentrations and residence times) to determine the conversion efficiency of each modelled RO$_2$ species to HO$_2$. The potential interference in the RO$_2$ measurements from HO$_2$NO$_2$ and CH$_3$O$_2$NO$_2$ has been explored in the Supplementary Information in section S1.4, however the data presented through-out the paper are the uncorrected data since the correction is small (correction from the decomposition of HO$_2$NO$_2$ and CH$_3$O$_2$NO$_2$ is ~6

185   %, ~8 % and 4 % for total, complex and simple RO$_2$, respectively.)

2.2.1.3 Inlet Pre Injector

For part of the campaign, an Inlet-pre-injector (IPI) was attached to the HO$_x$ cell. The IPI removes ambient OH by the injection of propane directly above the cell inlet and facilitates a background measurement whilst the laser wavelength is still tuned to an OH transition, with this type of OH

190   measurement known as "OHchem". The OHchem background signal will include a signal from laser scattered light, scattered solar radiation and may potentially also include a fluorescence signal from any OH that is generated internally from an interference precursor within the LIF cell. Internally generated OH constitutes an interference, but can be readily identified by comparing the OHchem background signal to the background signal measured when the laser wavelength is tuned away from

195   the OH transition, with this type of OH measurement known as "OHwave". The OHwave background signal is from laser scattered light and solar scattered radiation only. OHchem is the online OH signal – OHchem background and OHwave is the OH online signal – OHwave background.

The Leeds IPI was first implemented during the ICOZA campaign in Norfolk, UK, in the summer of 2015, and is described in further detail elsewhere (Woodward-Massey et al., 2019). During the APHH winter

200   campaign the laser online (wavelength tuned to the OH transition) period lasted 300 seconds for both OHchem and OHwave data acquisition cycles. When the IPI was physically taken off the HO$_x$ fluorescence cell, OH and HO$_2$ were measured sequentially in this cell with 150 seconds online period each. The other (RO$_x$) fluorescence cell measured HO$_2$* and RO$_2$ simultaneously with OH and HO$_2$, respectively, when the IPI was removed. When the IPI was being operated during the APHH campaign

205   OHwave, OHchem and HO$_2$ were measured in the HO$_x$ cell sequentially for 120, 120 and 60 seconds, respectively. The RO$_x$ cell measured HO$_2$* and RO$_2$ for 240 and 60 seconds, respectively when the IPI was operated. The laser offline period for both data acquisition cycles lasted 30 seconds, with NO injected for the final 15 seconds of this laser offline period. From the 08/11/2016 to 24/11/2016 the HO$_x$ cell was operated without the IPI assembly in place, the IPI was then installed and run on the HO$_x$

210   cell from 02/12/2016 to 08/12/2016.

The correlation of OHwave and OHchem during the APHH winter campaign is shown in Figure 3. The slope of 1.05±0.07 demonstrates that within the errors in the linear fit no interference was evident

during the winter campaign. OHwave data were corrected for the known interference from O_3 + H_2O, see Woodward-Massey et al. (2020) for further details. The O_3 + H_2O interference calculated was very small (median ~8.5 x 10^3 molecule cm^{-3}) due to the low concentration of H_2O and O_3. All figures and calculation from now on have used OHwave as it is 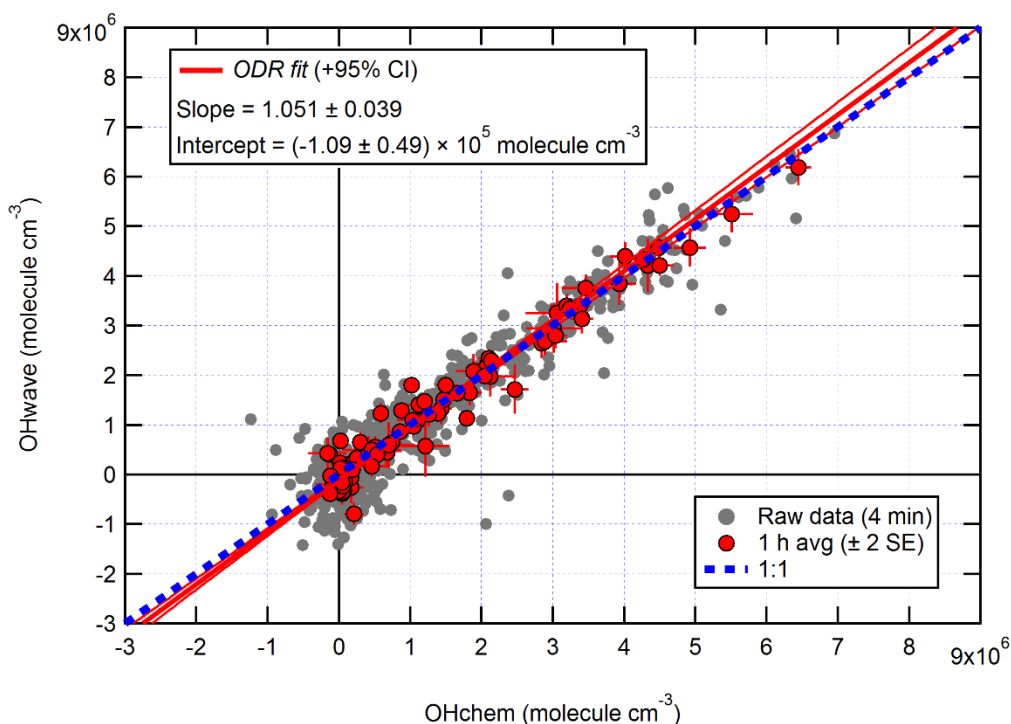the most extensive time-series (12 days compared to 5 days). All figures and calculation from now on have used OHwave as it is the most extensive time-series (12 days compared to 5 days).

Figure 3. Overall intercomparison of OHwave and OHchem observations from the winter 2016 APHH campaign. Grey markers represent raw data (6 min acquisition cycle, 4 minutes and 2 minutes for the OH and HO_2 measurements), with 1 h averages (±2 standard error, SE) in red. The thick red line is the orthogonal distance regression (ODR) fit to the hourly data, with its 95% confidence interval (CI) bands given by the thin red lines; fit errors given at the 2σ level. For comparison, 1:1 agreement is denoted by the blue dashed line. OHwave data were corrected for the known interference from O_3 + H_2O. Taken from (Woodward-Massey et al., 2020) where further details can be found.

2.2.2 Calibration

The instrument was calibrated approximately every three days by photolysis of a known concentration of water vapour at 185 nm in synthetic air (Messer, Air Grade Zero 2) within a turbulent flow tube to generate equal concentrations of OH and HO_2 as described in Whalley et al. (2018). The product of the photon flux at 185 nm and the water vapour photolysis time, which is required to calculate the concentration of OH and HO_2, was measured using a $N_2O \rightarrow NO$ chemical actinometer (Commane et al., 2010) both before and after the APHH campaign. For calibration of RO_2 concentrations, methane (Messer, Grade 5, 99.99%) was added to the humidified air flow in sufficient quantity to rapidly titrate OH completely to CH_3O_2. For reporting the total concentration of RO_2 the calibration factor for CH_3O_2

was used. More details on the RO_xLIF and calibration, for example the sensitivity of the instrument towards various RO_2 species which is taken into account when comparing RO_2 measurements to model calculations, can be found in Whalley et al. (2018). The limit of detection (LOD) on average for the APHH campaign was 5.5×10^5 molecule cm^{-3} for OH, 3.1×10^6 molecule cm^{-3} for HO_2 and 6.5×10^6 molecule cm^{-3} for CH_3O_2 at a typical laser power of 11 mW for a 7 minute data acquisition cycle (SNR=2). The field measurements of all species were recorded with 1 s time-resolution, and the precision of the measurements was calculated using the standard errors in both the online and offline points. The accuracy of the measurements was ~ 26 % (2σ), and is derived from the error in the calibration, which derives largely from that of the chemical actinometer (Commane et al., 2010).

2.2.3 OH Reactivity

OH reactivity measurements were made using the laser flash photolysis pump-probe technique and the instrument is described in detail in Stone et al. (2016). Ambient air was drawn into the reaction cell (85 cm in length, 5 cm in diameter) at 12 SLM. Humidified ultra-high purity air (Messer, Air Grade Zero 2) passed a low-pressure Hg lamp at 0.5 SLM to generate ~ 50 ppbv of O_3 which was mixed with the ambient air. The O_3 was photolyzed at 266 nm to generate a uniform OH concentration across the reaction cell. The change in the OH radical concentration from pseudo-first-order loss with species present in ambient air was monitored by sampling the air from the reaction cell into a FAGE detection cell at ~1.5 Torr. The 308 nm probe laser (same as the FAGE laser describe above) was passed across the gas flow in the FAGE cell to excite OH radicals, and then detected the fluorescence signal at ~ 308 nm detected by a gated channel photomultiplier tube. The OH decay profile owing to reactions with species in ambient air was detected in real time. The decay profile was averaged for 5-mins and fitted with a first-order rate equation to find the rate coefficient describing the loss of OH (k_{loss}), with k_{OH} determined by subtracting the physical loss of OH (k_{phys}). The OH reactivity data were fitted with a mono-exponential decay function as no bi-exponential behaviour was observed, even at the highest NO concentrations, and hence there was no evidence for recycling from HO_2 + NO impacting on the retrieved values The total uncertainty in the ambient measurements of OH reactivity is ~ 6% (Stone et al. 2016).

2.2.4 The Master Chemical Mechanism, MCM

A constrained zero-dimensional (box) model incorporating version 3.3.1 of the Master Chemical Mechanism (MCMv3.3.1) (http://mcm.leeds.ac.uk/MCM/home) was used to predict the radical concentrations and OH reactivity and to compare with the field observations. The MCM is a detailed mechanism that almost explicitly describes the oxidative degradation of ~ 140 VOCs ranging from methane to those containing 12 carbon atoms (C1 – C12). The complete details of the kinetic and

photochemical data used in the mechanism can be found at the MCM website (http://mcm.leeds.ac.uk/MCM/home). For this work, the model was run with a sub-set of the MCM and treated the degradation of simultaneously measured non-methane VOCs, CH_4 and CO following oxidation by OH, O_3 and NO_3, and included 11,532 reactions and 3,778 species. The model was constrained by measurements of NO, NO_2, O_3, CO, HCHO, HNO_3, HONO, water vapour, temperature, pressure and individual VOC species measured by GC-FID (gas chromatography with flame ionisation). The accuracy and precision of trace gas species can be found in Table 2, details on the HONO measurements used in the modelling scenarios can be found in Crilley et al.(2019). Details for other measurements can be found in Shi et al.(2018). The time resolution for the GC-FID data was 1 hr and has been interpolated to 15-min for the model input.

Table 1 shows the different species measured by the GC-FID whose degradation was included in the mechanism used. The model was constrained with the measured photolysis frequencies $j(O^1D)$, $j(NO_2)$ and $j(HONO)$), which were calculated from the measured wavelength-resolved actinic flux and published absorption cross sections and photodissociation quantum yields. For other species which photolyse at near-UV wavelengths, such as HCHO and CH_3CHO, the photolysis rates were calculated by scaling to the ratio of clear-sky $j(O^1D)$ to observed $j(O^1D)$ to account for clouds. For species which photolyse further into the visible the ratio of clear-sky $j(NO_2)$ to observed $j(NO_2)$ was used. The variation of the clear-sky photolysis rates (j) with solar zenith angle (χ) was calculated within the model using the following expression Eq. 1:

$$j = l \cos(\chi)^m \times e^{-n \sec(\chi)}$$ Eq. 1

with the parameters *l, m* and *n* optimised for each photolysis frequency (see Table 2 in Saunders et al. (2003).

A constant H_2 concentration of 500 ppbv was assumed (Forster et al., 2012). The model inputs were updated every 15 minutes, the species that were measured more frequently were averaged to 15 minutes whilst the measurements with lower time resolution were interpolated. The loss of all non-constrained, model generated species by deposition or mixing was represented as a first order deposition rate equivalent to 0.1/MH (MH represent the height of the boundary layer). The effect of changing the deposition rate is minor, as shown in Figure S1 of the Supplementary Information. The model was run for the entirety of the campaign in overlapping 7 day segments. To allow all the unmeasured, model generated intermediate species time to reach steady state concentrations, the model was initialised with inputs from the first measurement day (16th November 2016) and spun-up for 2 days before comparison to measurements were made. The model described above is from now on called MCM-base.

An additional model was run using higher weight VOCs that were measured using a PTR-MS (Proton Transfer Mass Spectrometer) to assess the effect on modelled radical species (OH, HO_2 and RO_2) and modelled OH reactivity, with this model run showing there is <10% effect on the radical concentration and OH reactivity (see Supplementary Information, Figures S2 and S3).

Instrument	Species	Reference
DC-GC-FID	Methane, Ethane, ethylene, propane, propene, isobutane, butane, C_2H_2, trans-but-2-ene, but-1ene, Isobutene, cis-but-2-ene, 2-Methylbutane, pentane, 1,3-butadiene, trans-2-pentene, cis-2-pentene, 2-methylpetane, 3-methypetane, hexane, isoprene, heptane, Benzene, Toluene, m-xylene, p-xylene, o-xylene, methanol, dimethyl ether.	Hopkins et al. (2011)

Table 1. VOC species measured by the DC-GC-FID (dual channel gas-chromatography with flame ionisation detection) that have been constrained in the box-model utilising the Master Chemical Mechanism.

Instrument	Technique	2σ Uncertainty / %	2σ Precision/ ppbv
O_3, TEi49i	UV absorption	4.04	0.28[1]
NO, TEi42i-TL	Chemiluminescence via reaction with O_3	4.58	0.03[1]
SO_2, TEi43i	UV fluorescence	3.12	0.03[1]
NO_2, CAPS, T500U	Cavity enhanced absorption spectroscopy	5.72	0.04[1]
HONO	LOPAP x2, BBCEAS x 2, ToF-CIMS and SIFT-MS	9 – 22%	0.025 – 0.130

Table 2. Instruments and techniques used to measure key model constraints. 2σ uncertainties for the measured trace gas species used in the modelling scenarios are quoted. [1]Precision is given for 15-minute averaging time. For details of the HONO measurements please see Crilley et al.(2019).

The model scenarios involved in this work are summarised in Table 3.

Model Name	Description
MCM-base	The base model described above in Section 2.2.3.
MCM-cHO$_2$	The same as MCM-base, but with the model constrained to the measured value of the HO_2 concentration.
MCM-PRO2	The same as MCM-base, but including an extra primary source of RO_2 species to reconcile the measured total RO_2 with modelled RO_2. Details for this can be found in section 4.2.
MCM-PRO2-SA	The same as MCM-PRO2 but including the uptake of HO_2 to aerosol with an uptake coefficient of γ = 0.2 Jacob et al.(2000).

Table 3. Description of the model scenarios and how they differ from the base model, and the associated name of that model that has been used in the body of this work.

3 Results

3.1 Chemical and Meteorological conditions

During the campaign various chemical and meteorological conditions were observed, as shown in Figure 4, including several haze periods. According to the meteorological standards (QX/T113-2010, Shi et al. (2018)), haze is defined as (i) visibility < 10 km at relative humidity (RH) < 80 % or (ii) if RH is between 80 and 95 %, visibility < 10 km and PM2.5 > 75 μg m^{-3}. For the purpose of this work the periods defined as haze are when $PM_{2.5}$ exceeds 75 μg m^{-3}. The wind rose for the winter 2016 campaign shows the dominant wind direction is from the northwest which coincides with higher wind speeds, also south westerly flows were frequent in the winter APHH campaign (see Shi et al. (2018) for more details). The south-westerly wind direction observed in the winter 2016 campaign had the potential to bring more polluted air from the upwind Hebei province to the observations site in Beijing.
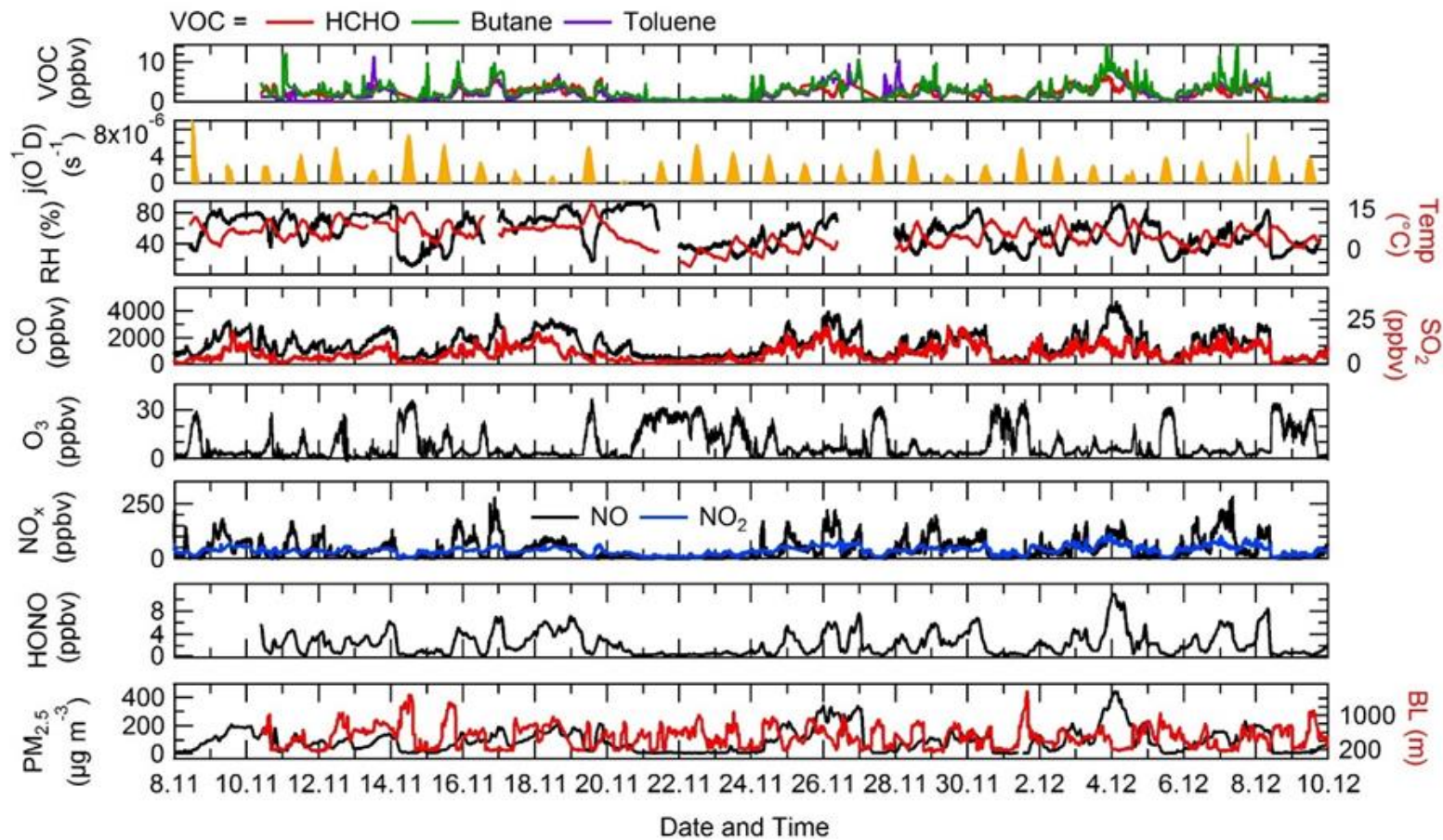
The timeseries of $j(O^1D)$, relative humidity (RH), temperature, CO, SO_2, O_3, NO, NO_2, HONO, $PM_{2.5}$, HCHO, butane and toluene is shown in Figure 4. There were several co-located measurements of HONO made during the APHH campaign, and the HONO mixing ratios shown in Figure 4 and used in the model were values taken from a combination of all measurement at the IAP site, and recommended by Crilley et al. (2019) who provide further details for the methodology for selection of the HONO data. For a given time of day, large variations in $j(O^1D)$ during the campaign were observed, with the reductions caused by decreasing light levels driven by enhanced $PM_{2.5}$. The temperature during the campaign varied between -10°C and +15°C. The relative humidity during the campaign varied between 20 – 80% RH; generally with higher RH coinciding with haze events. The time-series for trace gas species showed high mole fractions for CO (1000-4000 ppbv), SO_2 (5 – 25 pbbv), NO (20 – 250 ppbv) but relatively low O_3 (1 – 30 ppbv). HONO during the campaign was generally quite high reaching up to 10 ppbv (Crilley et al., 2019). Frequent haze events were also observed during the winter campaign, with $PM_{2.5}$ mass concentration reaching up 530 μg m^{-3}. The VOC concentration (HCHO, toluene and butane) track pollution events and each other very well; the mole fraction of the VOCs varied between 0.2 - 11.3 ppbv.

The diel variation for $j(O^1D)$, NO, NO_2, O_3, O_x, HONO, boundary layer height (BL) and CO separated into haze and non-haze periods is shown in Figure 5; the periods defined as haze are shown in Table 4. During the haze events $j(O^1D)$ decreased by ~50% at midday, as shown in Figure 5. The photo-activity of $j(HONO)$ and $j(NO_2)$ extends further into the visible region of the solar spectrum compared with $j(O^1D)$ and so the reductions in their photolysis rates within haze are less; ~40% for $j(HONO)$ and ~35% for $j(NO_2)$ as discussed in (Hollaway et al., 2019). During polluted and hazy periods NO on average reached 100 ppbv at 8 am; on some days NO was close to 250 ppbv, some of the highest levels ever recorded during an urban field campaign. On clearer days, the peak NO was ~ 40 ppbv at 8 am (CST).

A distinct increase in CO, NO_2 and SO_2 was also observed during haze periods, but no clear diurnal pattern in and outside of haze for these species was observed, as shown in Figure 5. The O_3 during the haze periods reduced on average by a factor of 3, due to titration by reaction with the high concentrations of NO observed. NO and O_3 show an anti-correlation during the cleaner periods due to their inter-conversion. The sum of NO_2 and O_3, O_x, increased during pollution periods from 40 ppbv to a maximum of 53 ppbv on average. HONO in both clean and haze periods shows a distinct diel pattern, with a large decrease in the morning from loss through photolysis and a minimum in the afternoon; a large increase in HONO concentration overnight probably originates from heterogeneous sources (i.e. NO_2 converting to HONO on humid surfaces) (Finlayson-Pitts et al., 2003; Lee et al., 2015; Li et al., 2012; Lu et al., 2018; Zhang et al., 2016b; Zhou et al., 2003). The HONO concentration was a factor of 3 higher on average during haze periods at midday than during the clearer periods. The boundary layer height (BLH) shows a similar diurnal variation inside and outside of haze, although the maximum BLH in haze is shifted to 14:30 compared to 12:30 outside of haze. The maximum and minimum BLH is similar inside and outside of haze and shows that containment is not the only driving force for pollution periods.

Haze Event	Local Time	$PM_{2.5}$ ($\mu g\ m^{-3}$)	Visibility (km)
Event 1	08/11 21:00 – 10/11 16:00	158 (79 – 229)	4.1 (2.3 – 8)
Event 2	15/11 21:00 – 19/11 08:00	143 (56 – 244)	4.2 (0.6- 8)
Event 3	24/11 12:00 – 27/11 02:00	210 (68 – 363)	4.2 (1.5 -8)
Event 4	02/12 16:00 – 05/12 02:00	239 (58 – 530)	3.9 (0.9 -8)
Event 5	06/12 09:00 – 08/12 10:00	144 (64 – 229)	4.6 (2.2 – 8)

Table 4. The different haze periods observed during the winter campaign. Table recreated from Shi et al. (2018), from which further details can be found.

368

Figure 4. Time-series of j(O^{1}D), relative humidity (RH), temperature (Temp), CO, SO$_2$, O$_3$, NO$_x$, HONO, boundary layer (BL), PM$_{2.5}$, HCHO, butane and toluene from the 8th of November to 10th December 2016 at Institute of Atmospheric Physics (IAP), Beijing.
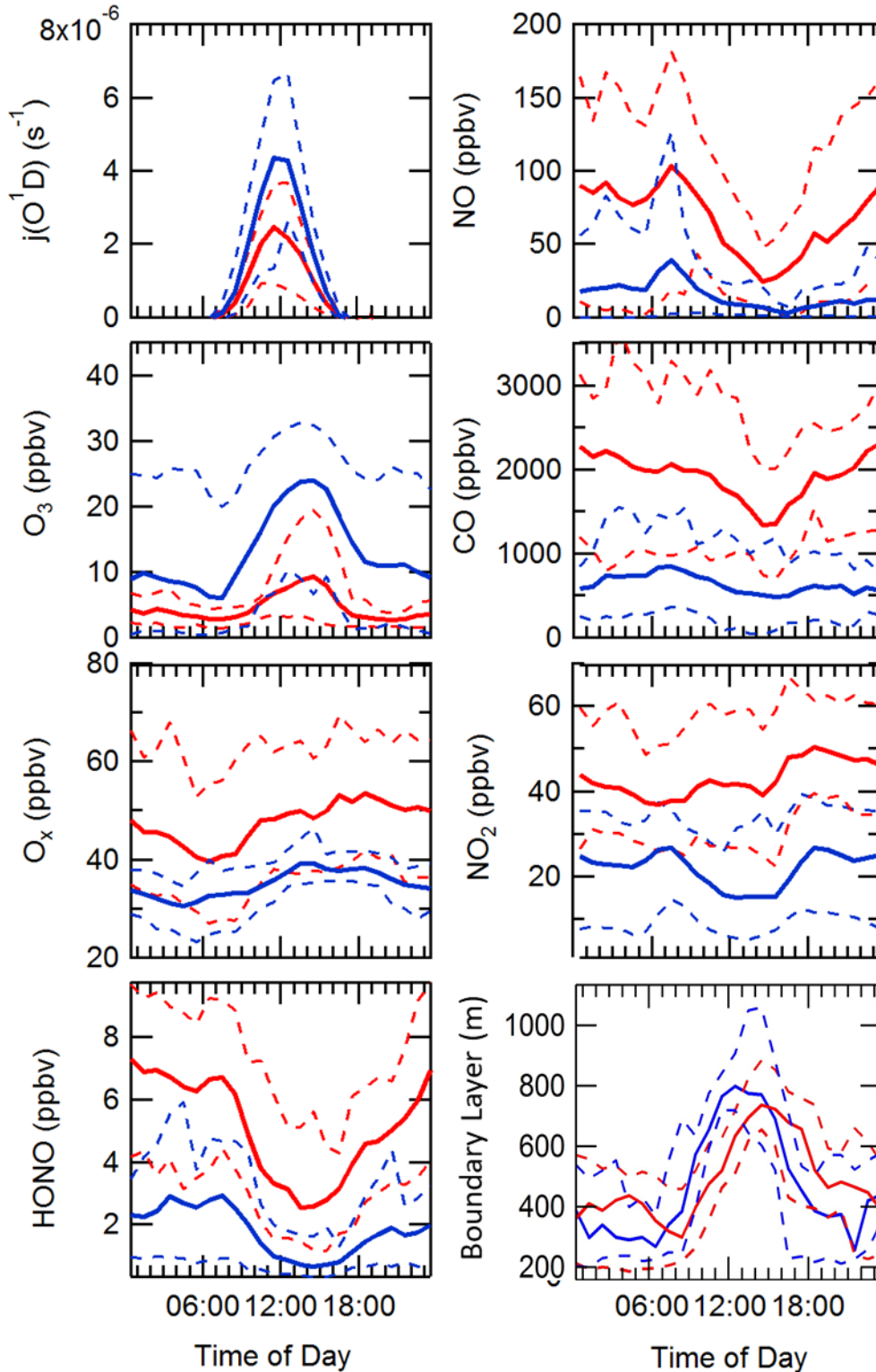
371

Figure 5. Comparison of the median average diel variation for $j(O^1D)$ (s^{-1}), NO (ppbv), O_3 (ppbv), CO (ppbv), O_x (ppbv), NO_2 (ppbv), HONO (ppbv) and boundary layer height (m) inside and outside haze events; denoted by solid red and blue lines, respectively. The dashed lines represent the interquartile range for the respective species and pollution period.

3.2 Steady State calculation of OH

380   Using measured quantities, a steady state approach has been used to calculate the OH concentrations for comparison with measurements, and also to determine the major sources of OH measured during the campaign. The photostationary steady state equation for OH, obtained from $d[OH]/dt = 0$, is given by a balance of the rate of production and the rate of destruction of OH:

$$[OH]_{pss} = \frac{p(OH) + j(HONO)[HONO] + k[HO_2][NO]}{k(OH)}$$
    Eq. 2

where p(OH) is the measured rate of OH production from ozone photolysis and the subsequent

385   reaction of $O(^1D)$ with water vapour, k is the rate coefficient for the reaction of HO_2 with NO at the relevant temperature, and $k(OH)$ is the measured OH reactivity. Equation (2) is a simplification, and only takes into account the production of OH from two photolysis sources (O_3 and HONO) and from the reaction of HO_2 + NO. O_3+alkene and $HO_2 + O_3$ reactions are not included as, owing to the generally low ozone experienced, these were found to contribute < 1 % to the total OH production, as discussed

390   in the MCM modelling section below. The pseudo-first order rate of loss of OH was constrained using the measured OH reactivity during the campaign, and hence includes all loss processes for OH.

Figure 6 shows the steady state calculation for OH between 2/12/2016 to 8/12/2016 where it is compared with the measured OH concentrations. These days were chosen as full data coverage for HONO, NO, j values, radical and $k(OH)$ measurements were available. The agreement between the

395   observed OH and OH calculated by equating the rate of OH produced from HO_2+NO and HONO photolysis and the loss of OH by reaction with all of its sinks, Eq.2, is very good. The agreement highlights that the OH budget can be determined by field measurements of the parameters necessary to quantify its rate of production and loss, and is closed to within 10%, well within the 26% error on the OH measurements themselves. The closure of the experimental budget suggests that measured

400   OH and HO_2 are internally consistent, and that just from measured quantities the rate of production and the rate of destruction are the same within uncertainties. Although on the 04/12/2016 the PSS overpredicts the measured OH by a factor of ~2.5, the differences between the PSS and measured OH could be due to a variety of reason including errors in OH, HO_2, NO, kOH and HONO measurements and NO segregation across the site. A further discussion for the PSS for the 04/12 can be found in the

405   Supplementary Information section S1.6. The reaction of HO_2 and NO is the dominant source of OH ($\sim 80 - 90\%$) for Beijing during wintertime, owing to NO being so high in concentration. The photolysis of HONO is the second most important source producing $\sim 10 - 20\%$ of OH (and a much larger primary source of radicals in general as discussed below). The PSS has been separated into haze and non-haze events and shows that during haze events the PSS captures the OH concentration, although the PSS

410   does overpredict the OH concentration by ~1.35 between 09:30 – 14:30 in haze events. However, the

overprediction by the PSS in haze events is highly influenced by the overprediction on the 04/12/2016. Whilst under non-haze conditions the PSS captures the OH concentration very well throughout the day. The production of from HONO increases in non-haze (~19%) compared with haze events (~7%). Due to low concentrations of O_3 in winter, the photolysis of O_3 and the subsequent reaction of $O(^1D)$ with water vapour is not an important source, being < 1 % of the rate of production. In addition, the reaction of O_3 with alkenes (whose concentrations were elevated in the winter) also contributed < 1% to the rate of OH production. The different HONO measurements present during the APHH campaign varied up-to ~40%, the sensitivity of the PSS on measured HONO is shown in the Supplementary Information section S1.5.
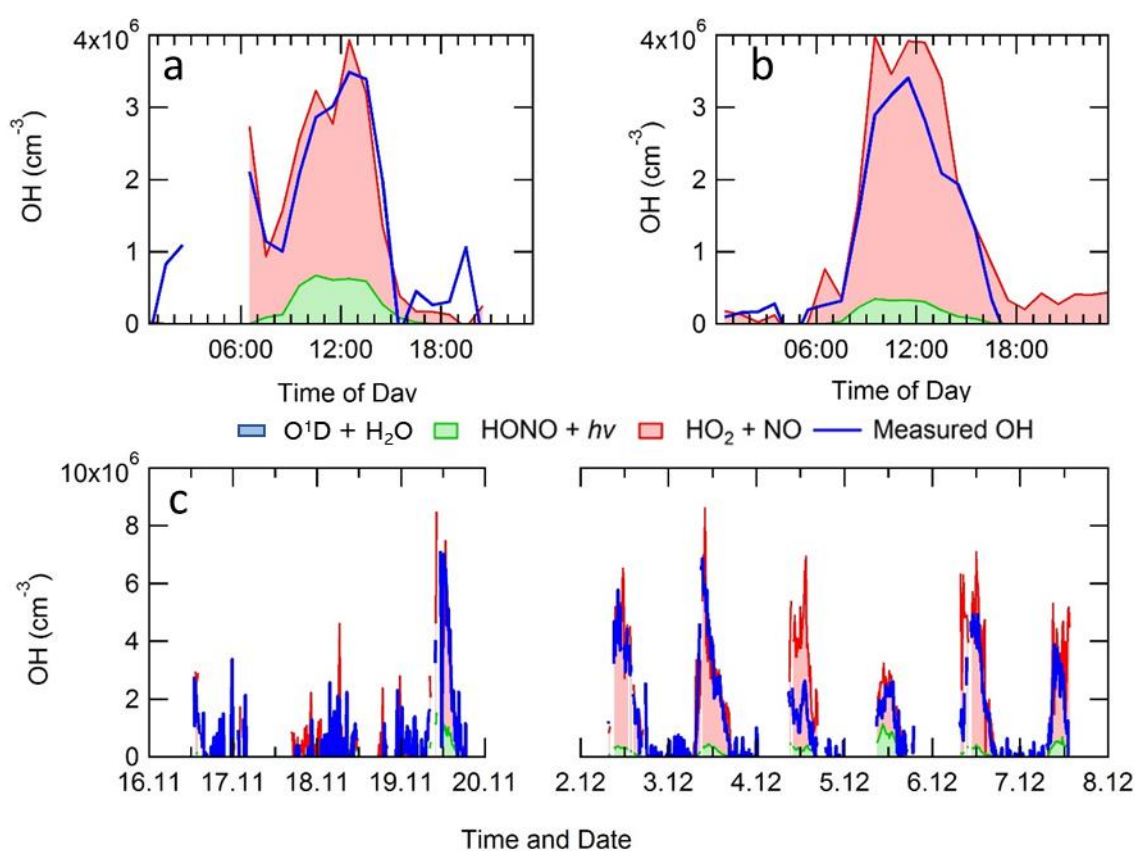

Figure 6. Average diel profile for observed and steady state calculated OH concentrations for: (a) non-haze, and(b) haze periods. Panel (c) shows a comparison time-series for the steady state calculation of OH and measured OH. The OH generated by O^1D+H_2O, although included in the key, is too small to be visible.

3.3 Comparison of measured OH, HO_2, RO_2 radical concentrations and OH reactivity with calculations using a box-model and the Master Chemical Mechanism

Figure 7 shows a comparison between measured and modelled (MCM-base, defined in Table 3) OH, HO_2, RO_2 (speciated into simple and complex RO_2, defined in section 2.2.1) and OH reactivity. As seen in Figure 7, the measured daily maximum for the radical species varied day-to-day over the range 2.5 to 8 x 10^6 cm^{-3}, 0.07 to 1.5 x 10^8 cm^{-3} and 0.8 to 2 x 10^8 cm^{-3} for OH, HO_2 and sum of RO_2 respectively.

The daily maximum concentration for the sum of simple RO_2 varied between 0.2 to 1.3 x 10^8 cm^{-3}, and the complex RO_2 daily maximum concentration varied between 0.2 and 0.6 x 10^8 cm^{-3}. On average, the model underpredicts the OH, HO_2 and RO_2 concentrations by a factor of 1.7, 5.8 and 25, as shown in Figure 8. Although the underprediction by the model varies day-to-day: for OH, the underprediction varies from a factor of 5.9 to an overprediction of 1.05 (showing good agreement) between the model and measurements; for HO_2 the underprediction varies from a factor of 13.6 to an over prediction by a factor of 5.3 and for RO_2 the under prediction varies from a factor of 2.1 to an over prediction of 8.0. Figure 8 shows the diel profile of OH, HO_2 and RO_2 averaged over the campaign, with daily average maximum of 2.7 x 10^6 cm^{-3}, 0.39 x 10^8 cm^{-3} and 0.88 x 10^8 cm^{-3} for OH, HO_2 and total RO_2, respectively. The complex and simple RO_2 show a very similar diurnal profile both peaking at 12:30 at a concentration of 4.4 x 10^7 molecule cm^{-3} and 4.5 x 10^7 molecule cm^{-3}, respectively. The model underpredicts the simple and complex RO_2 at 12:30 by a factor of 30 and 22, respectively. The large underprediction of both simple and complex RO_2 highlights the needs for additional primary sources forming both simple and complex species in the model. Section 4.2 explores the impact of additional primary source of RO_2 added into the model on OH and HO_2. The total measured OH reactivity during the campaign was quite large and varied between 10 to 145 s^{-1}. Averaged over the full campaign period the contributions to reactivity came from CO (17.3%), NO (24.9%), NO_2 (22.1%), alkanes (3.0%), alkynes and alkenes (10.8%), carbonyls (5.7%), terpenes (3.7%) and modelled intermediates (6.77%). Unusually, the largest contribution to OH reactivity is from reaction with NO. As shown in Figure 7 and Figure 8, OH reactivity is reproduced within 10% implying that the OH reactivity budget is captured well by the model. The model OH reactivity is the sum of all measured and modelled intermediate species multiplied by the respective rate coefficient for their reaction with OH.

Consistent with the steady state calculation, and as shown also in Figure 8, when the box-model was constrained to the concentrations of HO_2 measured using FAGE in the field (from now on this model scenario is called MCM-cHO$_2$), the measured and modelled OH concentration are in agreement within 10% which is less than the 26% error on the OH measurements. MCM-cHO2 also increases the RO_2 concentration by ~3.5 compared to MCM-base, but the RO_2 is still underpredicted by a factor ~7. The HO_2 was constrained in the model by inputting the HO_2 concentration at every 15 minute time-step.
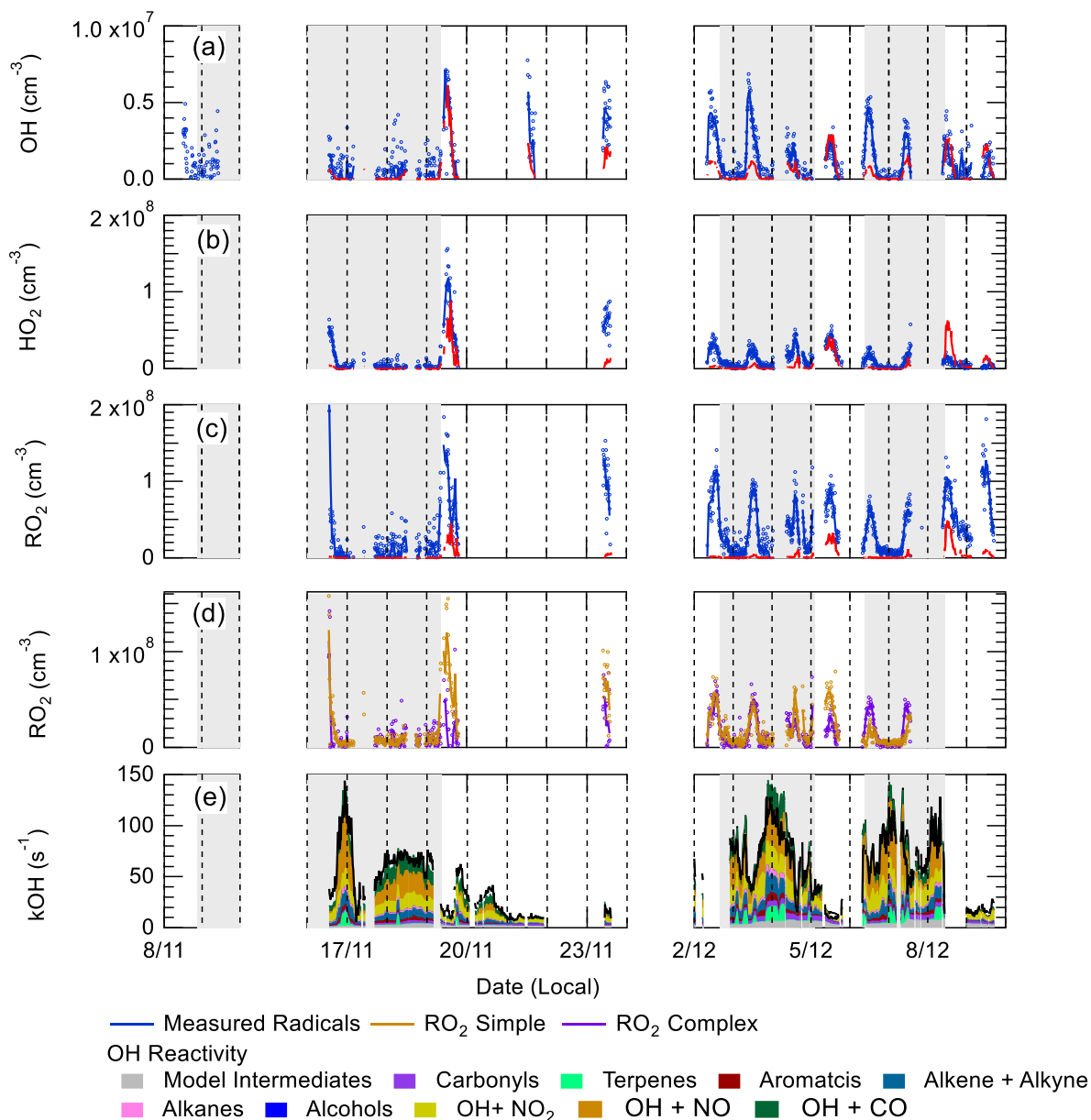
Figure 7. Time-series of OH, b) HO$_2$, c) total RO$_2$, d) partly-speciated RO$_2$ and e) measured (black) and modelled (stacked plot) OH Reactivity. For (a)-(c), the raw measurements (6-min data acquisition cycle) are blue open circles with 15 min average represented by the solid blue line. The 15 min model output in a-c is represented by the red line for OH, HO$_2$ and RO$_2$. The partly-speciated RO$_2$ is separated into simple (gold open circles) and complex (purple open circles)The individual contributions of the model to the OH reactivity is given below the graph. The grey shaded areas show the haze periods when PM$_{2.5}$ > 75 μg m^{-3}.
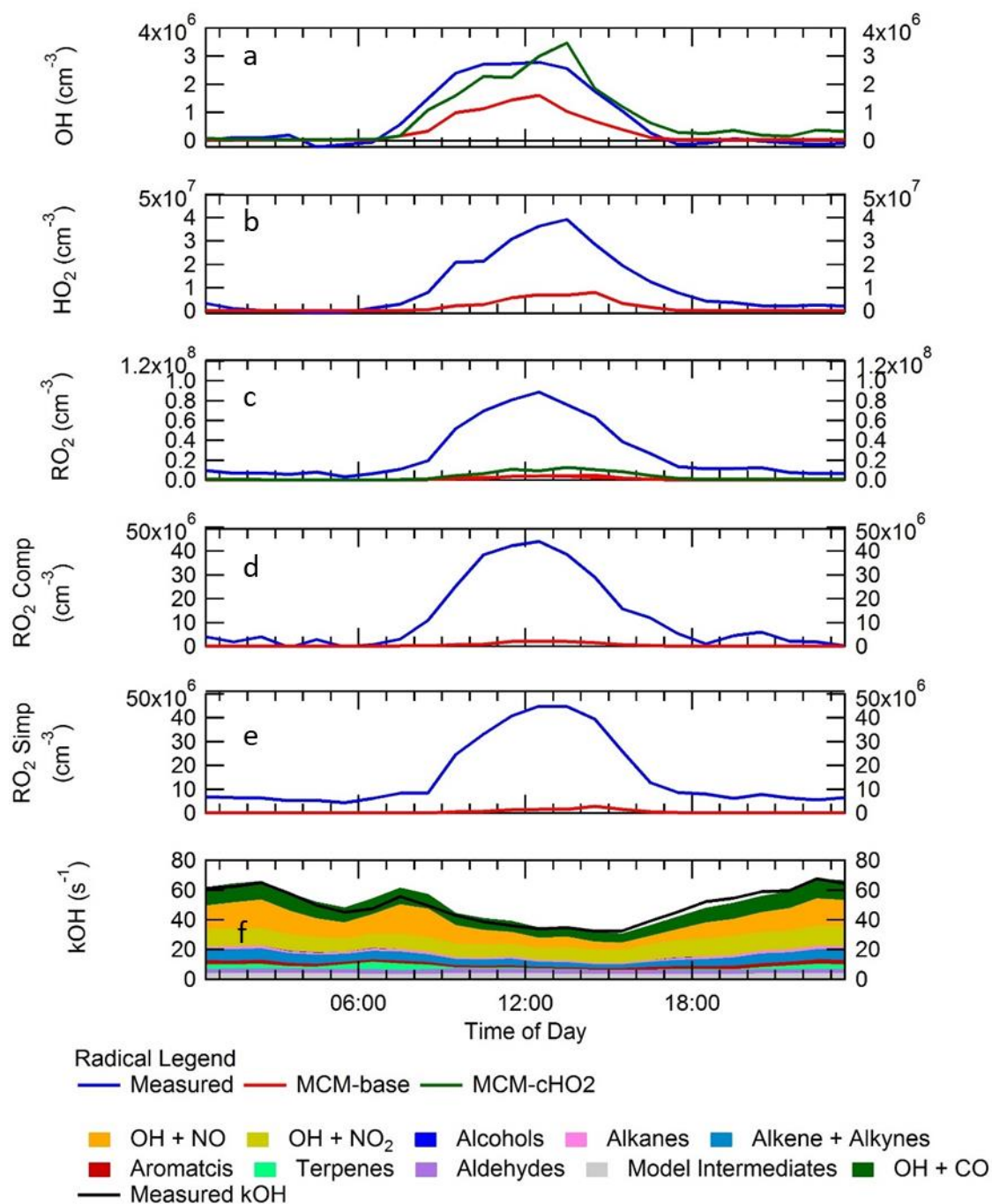
Figure 8. Campaign averaged diel profile of OH (a), HO_2 (b), sum of RO_2 (c), complex RO_2 (d), simple RO_2 (e) for measurements (blue) and box-model calculations: MCM-base (red) and MCM-cHO_2 (green). See text for descriptions of each model scenario. (f) – OH reactivity (s^{-1}) for measurements (black line) and model (stacked plot) with the contribution to reactivity from different measured species and modelled intermediates shown in the key.

The ability of the model to reproduce (to within ~10%) both the OH reactivity and the OH concentration when constrained to measured HO_2 (in MCM-cHO_2), but not to reproduce RO_2 radicals (whether constrained or not to HO_2) is suggestive of an incomplete representation of the chemistry of RO_2 radicals in the winter Beijing environment. The significant model underprediction of RO_2 implies either that additional sources of RO_2 radicals are required, or that it is inaccuracies in the recycling

chemistry within RO_2 species which leads to an overestimate of the loss rate of RO_2 under the high NO_x conditions experienced in central Beijing. The cause of the model underprediction of RO_2 is explored further in section 4.

As summarised in Table 5, previous winter campaigns, where the environment controlling peroxy radicals is generally dominated by NO, have shown a similar underprediction of radical species at high levels of NO_x (above 3 ppbv of NO) (Lu et al., 2013; Ma et al., 2019; Tan et al., 2017; Tan et al., 2018). For the BEST-ONE campaign, which took place in suburban Beijing (~60 km from the centre) it was suggested that in order to reconcile the model with the measurements, an additional source of RO_2 was required.

The OH concentrations measured are surprisingly high for a winter campaign where photolysis rates and RH are low; the average 12:00 OH maximum for the campaign was 2.7×10^6 molecule cm^{-3}. Comparisons with the level of agreement between measured and modelled radicals for other winter field campaigns are given in Table 5. The OH concentration is ~ 3, 2.3, 2, 1.65 and 1.5 times larger than winter measurements in New York (Ren et al., 2006), Beijing (Ma et al., 2019), Tokyo (Kanaya et al., 2007), Birmingham (Emmerson et al., 2005) and the BEST-ONE (Tan et al., 2018) campaigns, respectively, and similar to the campaign in Boulder (Kim et al., 2014). However, it should be noted that the Boulder campaign took place at a time in the year (late February/March) closer to mid-summer when there are higher light levels and water vapour (see Table 5 for details). As shown in Figure 7, the elevated OH concentrations inside haze events, for example up to 6×10^6 molecule cm^{-3} of OH was observed on 03/12/2016, suggests gas-phase oxidation is still highly active (this is explored more in section 4.3 and 4.4).

Campaign	Months, Year	NO (ppbv)	O$_3$ (ppbv)	OH Measured (10^6 cm^{-3})	OH Obs/ Model	HO$_2$ Measured (10^8 cm^{-3})	HO$_2$ Obs/ Model	RO$_2$ Measured (10^8 cm^{-3})	RO$_2$ Obs/ Model	Notes	References
APHH, Central Beijing, China	Nov – Dec, 2016	60	12	2.7	0.58	0.39	0.17	0.88	0.04	Average midday.	This work.
BEST-ONE Suburban Beijing, China	Jan – March, 2016	7	30	2.2	0.5	0.5	0.4	0.7	0.2	Campaign Median, midday, polluted period	Tan et al. 2018
NACHTT Boulder, USA	Late Feb, 2011	7	37	3	0.9	-	-	-	-	Average midday	Kim et al. (2014)
PUMA, Birmingham, UK	Jan-Feb, 2000	10	13	2	0.50	3	0.49	-	-	Average midday	Emmerson et al. (2005)
IMPACT Tokyo, Japan	Jan-Feb, 2004	8.1	35	1.5	0.93	0.27	0.88	-	-	Average midday	Kanaya et al. (2007)
PMTACS-NY2001 New York, US	Jan–Feb, 2004	25	20	1	0.83	0.17	0.17	-	-	Average midday	Ren et al. (2006)
PKU	Nov – Dec, 2017	30	10	1.4	1.4	0.3	0.13	-	-	Average Midday, Polluted period	Ma et al. (2019)

Table 5. Previous field measurements of OH, HO$_2$ and RO$_2$ that have taken place during wintertime in urban areas, together with the campaign average observed to modelled ratio. Modified from Kanaya et al. (2007).

4 Discussion

4.1 Sources and sinks of RO_x radicals

As shown in Figure 9, primary production of new radicals (radicals defined as RO_x = OH + HO_2 + RO + RO_2) via initiation reactions was dominated by the photolysis of HONO (68%, averaged over the campaign), with a small contribution from the photolysis of HCHO (2%), photolysis of carbonyl species (8%) and ozonolysis of alkenes (21%). An increased rate of production of RO_x radicals is observed during haze events, which is counterbalanced by an increase in the rate of termination. Figure 9 shows that alkene ozonolysis does not play an important role in production of RO_x radicals at night and is reflected by little to no OH observed during night-time as shown in Figure 8 (a). Similarly ozone photolysis does not appear to play an important role for the formation of OH, due to the low O_3 during the campaign, presumably a consequence of local titration via NO, as shown in Figure 4 and Figure 5. In addition, the low temperatures observed during winter caused a low water vapour concentration (~0.5 % mixing ratio), and hence the fraction of O^1D formed from the photolysis of ozone and which reacts with water vapour to form OH compared with collisional quenching (by N_2 and O_2) to form $O(^3P)$ was also low, and varied between 1% to 7% throughout the campaign. Figure 9 shows that almost all of the RO_2 species in the model are derived from OH sources highlighting the need for additional primary RO_2 sources in the model.
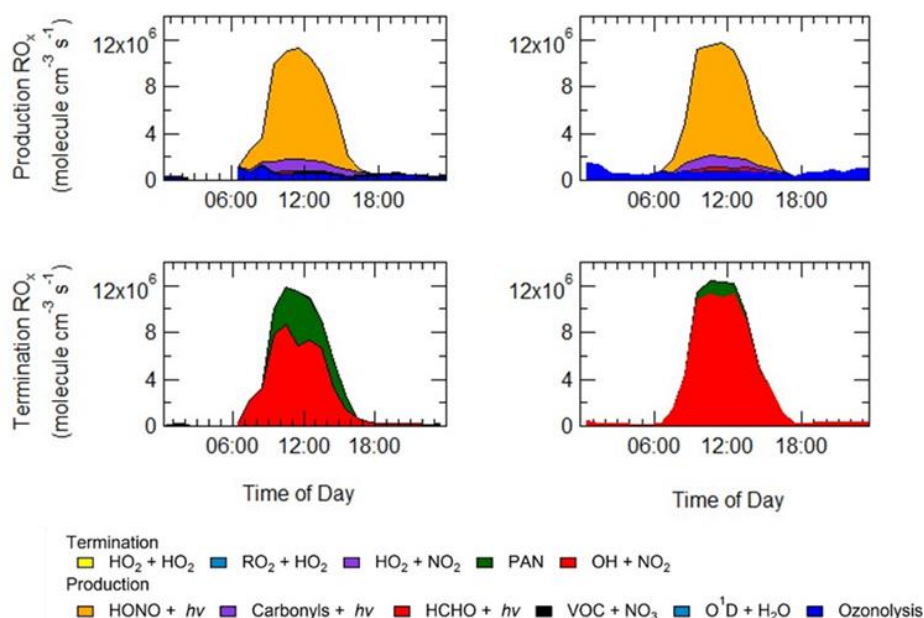

Figure 9. Rates of primary production (top panel) and termination (bottom panel) for RO_x radicals (defined as OH + HO_2 + RO + RO_2) calculated for MCM-base model separated into haze (right) and non-haze (left) periods. The definition of haze is when $PM_{2.5}$ exceeds 75 μm^{-3}. The production from: O^1D + H_2O and VOC + NO_3 and the termination reactions: RO_2 + HO_2, HO_2 + HO_2, HO_2 + NO_2, although shown in the key, are not visible and contributed <1% of the total production and termination.

The importance of HONO photolysis as a source of OH has been highlighted in several previous studies in both urban and suburban sites as summarised in Table 5.

The BEST-ONE campaign, 60 km north of Beijing, showed HONO produced ~ 46 % of the RO_x during the campaign, although in comparision to the APHH campaign, ozonolysis and carbonyl photolysis in BEST-ONE made up a more significant portion of primary production of radicals, 28 % and 9 %, respectively. The larger contribution to primary production from ozonolysis during BEST-ONE is probably due to higher ozone concentrations (3 times higher at midday, Figure 9). Both the APHH and BEST-ONE campaigns showed that ozone photolysis followed by the reaction of $O(^1D)$ atoms was not an important source of new radicals. A comparison between the primary production routes observed during the APHH and previous urban winter campaigns can be found in the Supplementary Information section S1.2.

In both haze and non-haze conditions, the two key reactions which caused a termination of the radical cycling chain reaction was from OH + NO_2. Figure 9 shows that OH + NO_2 contributes up to 94% and 65% in haze and non-haze, respectively. Figure 9 shows that during non-haze conditions contribution to termination from the net formation of PAN (~35%) becomes important; but under haze conditions less than 6% of RO_x termination comes from the net formation of PAN. In comparison to the BEST-ONE campaign, during the clean periods (clean periods are defined as times when $kOH < 15$ s^{-1}), the termination reactions of OH + NO_x, net-PAN and peroxy self-reaction contributed ~ 55%, 8%, 30% respectively (Tan et al., 2018). During the polluted periods in the BEST-ONE campaign, the termination reaction of OH + NO_2 increased to 80%, and the net-PAN formation and peroxy self-reaction decreased to ~ 12% annd 6% respectively. The BEST-ONE campaign shows very similar trends to the APHH campaign, except the APHH campaign shows a higher contribution to termination from OH + NO and OH + NO_2 even under cleaner periods. This is potentially due to the higher NO values observed during APHH (located in central Beijing ~6.50 km from Forbidden City) campaign compared to the BEST-ONE campaign. The work that took place at Peking University (PKU) (Ma et al., 2019) in Beijing (~11 km from the Forbidden City) shows a very smilar trend to the APHH campaign with 86% of the primary production of radicals produced from the photolysis of HONO during the polluted periods . The PKU campaign also showed <1% production from O^1D + H_2O, whilst small contribtions from ozonlysis (6%) and photolysis of carbonyls (including HCHO, ~7%) during the polluted periods. Similar to the APHH campaign, the termination of radicals during the PKU campaign during the polluted periods was dominated by the OH + NO (55%) and OH + NO_2 (43%), whilst there was a small contribtuion (~2%) from the net-formation of PAN. The termination trend is very similar to the APHH campaign.

24

4.2 Dependence of radicals concentrations with NO$_x$

560   Figure 10 shows the ratio of measured-to-modelled OH, which is close to 1 at or below 10 ppbv of NO; similar to the BEST-ONE campaign. Above 6 ppbv of NO the model underpredicts the OH concentration. As shown in Figure 10, at ~6 ppbv of NO; HO$_2$ and RO$_2$ are underpredicted by a factor of 5.4 and 18, respectively; similar peroxy radical under-predictions were reported from the BEST-ONE campaign (Tan et al., 2017; Tan et al., 2018), with HO$_2$ and RO$_2$ being underpredicted by a factor of 5

565   and 10 at 6 ppbv. Many previous urban campaigns have a more extensive data coverage at lower NO$_x$ values due to the smaller levels of NO$_x$ observed; however, no other campaign with *in situ* measurements of OH has experienced NO values up to 250 ppbv as observed during APHH. Figure 10 shows that the measured-to-modelled ratio for OH, HO$_2$ and RO$_2$ increases with NO concentration; for OH the ratio initially increases and then plateaus above 30 ppbv. There have been some suggestions

570   for the origin of the discrepancy that is observed between modelled and measured concentrations of radicals at high concentrations of NO. Dusanter et al., (2009) suggest that poor mixing of a point source of NO with peroxy radicals across a site may cause some of the model to measurement discrepancy observed. There were several instruments for NO measurements located around the site and no differences in concentrations were observed, hence no evidence of any obvious segregation. Tan et

575   al., (2017) suggest that there may be a missing source of peroxy radicals under high-NO$_x$ conditions. Alternatively, the measured-to-modelled discrepancy could be driven by unknown oxidation pathways of the larger, more complex, RO$_2$ species that are present in these urban environments, whose laboratory kinetics are under-studied.

   When the MCM is constrained to the measurements of HO$_2$ (MCM-cHO$_2$), the model can replicate the

580   OH measurements to ~10%, within the 26% error of the measurements, as shown in Figure 8. In addition, the MCM-base model can replicate the OH reactivity within 10 % (Figure 8), implying that almost all of the major sources and sinks of OH are captured. The underestimation of HO$_2$ by the model could be explained by the underestimation of RO$_2$ by the model, owing to an insufficient rate of recycling of RO$_2$ to HO$_2$. Both the ability to replicate OH when the model is constrained to HO$_2$, along

585   with OH reactivity being captured well by the model, suggests the presence of unknown RO$_2$ chemistry; either additional sources of RO$_2$ radicals under high levels of NO$_x$ or unknown chemistry/behaviour of RO$_2$ under high levels of NO$_x$. Indeed, many rate coefficients in the MCM for the more complex RO$_2$ species are based on structure activity relationships (SARs) determined from studies of simpler RO$_2$ species (http://mcm.leeds.ac.uk/MCM/home, Jenkin et al. (2019)). During the

590   APHH campaign, measurements of partially speciated RO$_2$ species were made: RO$_2$ simple (deriving from alkanes up to C$_3$) and RO$_2$ complex (deriving from alkanes > C$_4$, alkene and aromatics), see experimental section 2.2.1 for details on RO$_2$ speciation and (Whalley et al., 2013). The dependence

of the concentration of speciated RO_2 measurements against [NO], as shown in Figure 11, highlights that the concentration of complex RO_2 species has a steady decrease across the NO range, whilst the concentration of simple RO_2 species starts to decrease rapidly above 2.5 ppbv.The chemistry of the simpler RO_2 species with NO should be well understood, owing to a more extensive laboratory database of the rate coefficients and product branching, so the model discrepancy for RO_2 species may be due to inaccuracies within the MCM for the degradation of the more complex RO_2 species into these simple RO_2. The degradation pathways of the complex RO_2 species appear not to be well understood, and may be the reason why the real concentration of simple RO_2 species remain high even under high NO_x conditions, whereas the modelled simple RO_2 concentration decreases at high NO. The effect on reducing the RO_2 has been investigated and is shown in S1.7 in the Supplementary Information. The results show that reducing the rate constant by a factor ~10 does improved the modelled to measurements agreement by a factor of 8.3 for total RO_2. However, RO_2 is still underpredicted by a factor of ~12 at the highest NO. Also the increased RO_2 in the model does not recycle into HO_2 or OH efficiently. This work highlights that uncertainties in the rate constant for RO_2 + NO for different RO_2 cannot be the only explanation for the underprediction of RO_2 in the model.
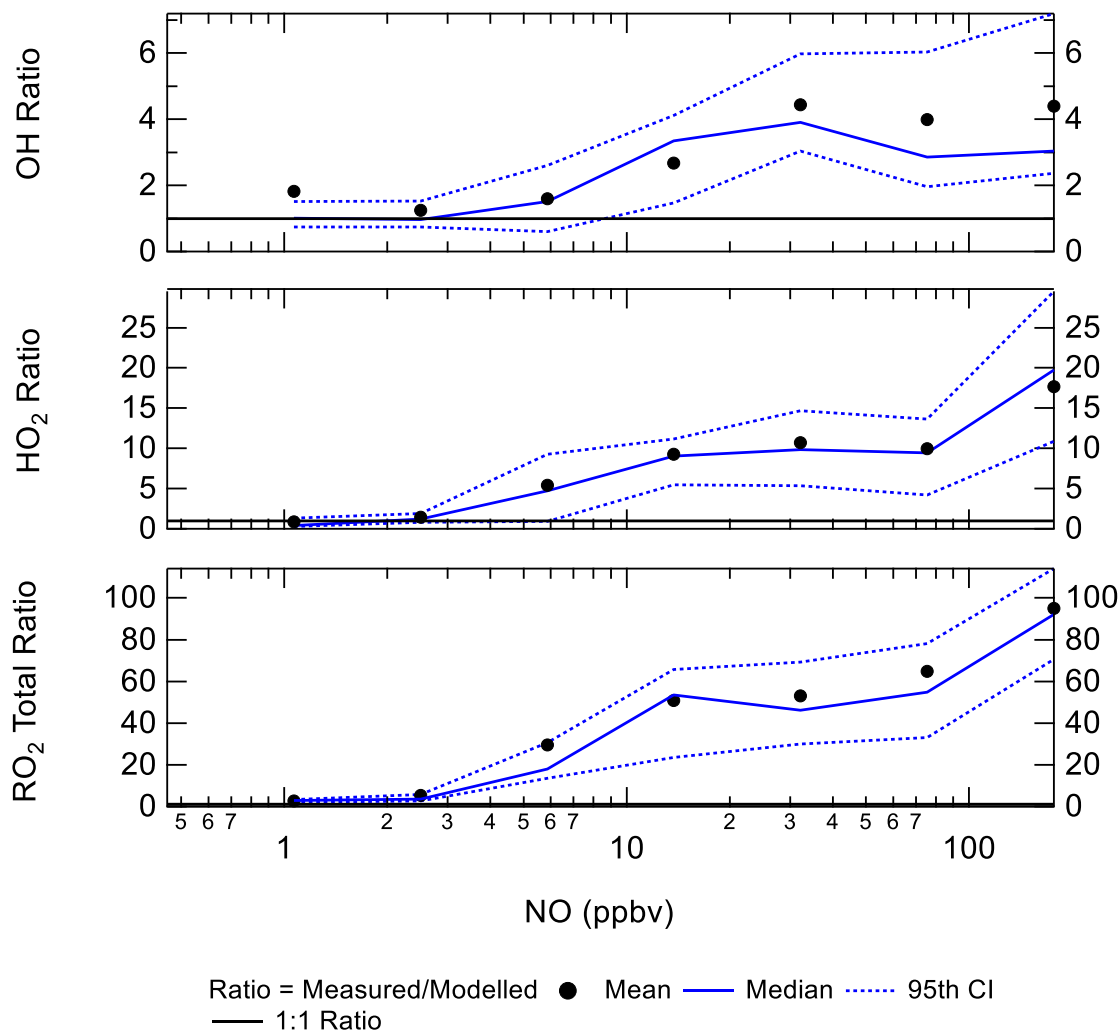
Figure 10. The ratio of measurement/model for OH (top), HO_2 (middle) and total RO_2 (bottom) across the range of NO concentrations experienced, for daytime values only ($j(O^1D) > 1 \times 10^{-6}$ s^{-1}). CI = Confidence Interval.
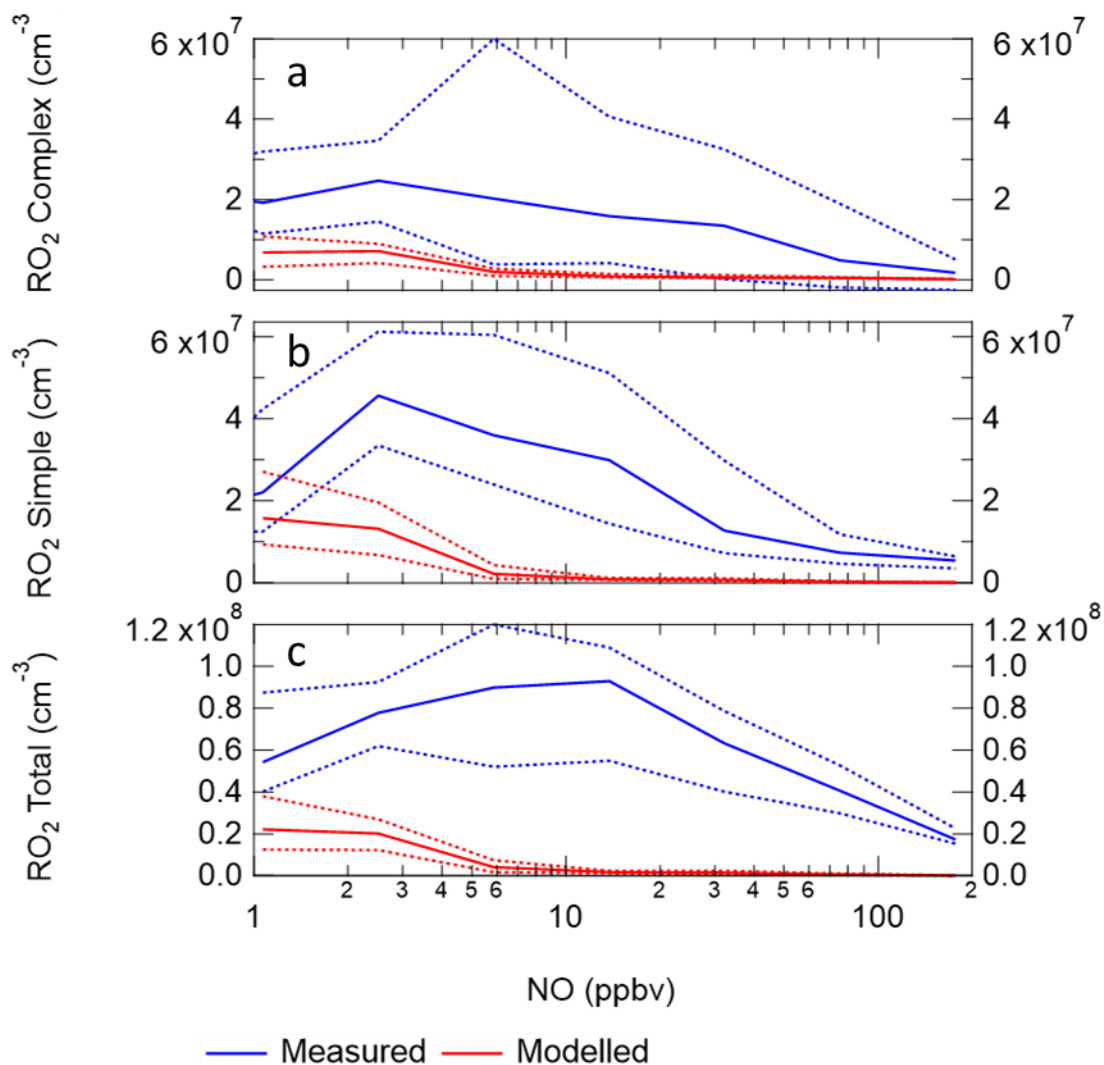
Figure 11. a – Complex RO_2 measurements (blue) and complex RO_2 modelled (black) versus NO. b – Simple RO_2 measurements (blue) and simple RO_2 modelled (black) versus NO. c – Total RO_2 measurements (blue) and total RO_2 modelled (black) versus NO. The points used are for daytime values only ($j(O^1D) > 1 \times 10^{-6}$ s^{-1}). See text for definition of "simple" and "complex" RO_2.

The additional primary production of RO_x (P'RO_x) radicals required to bridge the gap between measured and modelled total RO_2 was found to peak at an average of 3.5 $\times 10^8$ molecule cm^{-3} s^{-1} at 08:30 non-haze events. Under haze conditions, the gap between measured and modelled total RO_2 was found to peak at an average of 4 $\times 10^8$ molecule cm^{-3} s^{-1} at 13:30 as shown in Figure 12, calculated from Eq. 3 (Tan et al., 2018):

$$P'(RO_x) = k_{HO2+NO} [HO_2] [NO] - P(HO_2)_{prim} - P(RO_2)_{prim} - k_{VOC}[OH] \qquad \text{Eq. 3}$$
$$+ L(HO_2)_{term} + L(RO_2)_{term}$$

where $P(HO_2)_{prim}$, $P(RO_2)_{prim}$, $L(HO_2)_{term}$ and $L(RO_2)_{term}$ are the rates of primary production of HO_2, primary production of RO_2, termination of HO_2 and termination of RO_2, respectively. The overall

28

additional primary production peak at ~44 ppbv hr^{-1} (at 10:30) which is almost nine times larger than the additional RO$_2$ source that was required to resolve the measured and modelled RO$_2$ during the BEST-ONE campaign (5 ppbv h^{-1} during polluted periods, also calculated using Eq. 3), and is much larger compared to the known noon-average modelled primary production of RO$_x$ during the APHH campaign of 1.7 ppbv hr^{-1}. The additional primary production required in non-haze rises sharply in the morning peaking at 08:30 (3.5 x 10^8 molecule cm^{-3}) and then decreases rapidly; whilst the additional source needed in haze events peaks at 4 x 10^8 molecule cm^{-3} s^{-1}. The additional primary source required during haze events through-out the day is ~7 times higher than that during non-haze events. It has been suggested previously in Tan et al. (2017) that the missing primary radical source originates from the photolysis of ClNO$_2$ and Cl$_2$ to generate Cl atoms, which can further oxidise VOCs to generate peroxy radicals. However, as no measurements of ClNO$_2$ or Cl$_2$ measurements were made during the campaign, this route cannot be quantified. However, Cl atom chemistry may only play a minor role, as the inclusion of ClNO$_2$ in a model during a summer campaign in Wangdu (60 km from Bejing) could only close 10 – 30% of the gap between the model and measurements (Tan et al., 2017). Although the ClNO$_2$ concentration required to bridge the gap between model and measurements would be ~5800 ppbv on average (see Supplementary Information section S1.8 for details). Previous measurements in China in suburban Beijing have shown ClNO$_2$ peaking at 2.9 ppbv (Wang et al. 2017), however, and suggests other additional primary source are needed in the model besides Cl chemistry.

Eq.3 has been used to calculate an additional primary source ($P'(RO_x)$) required to reconcile measured and modelled RO$_2$; on average this peaked at 1.05 x 10^8 molecule cm^{-3} s^{-1}. The calculated additional RO$_2$ ($P'(RO_x)$) source was included in the model (model run is called MCM-PRO2) as a single species 'A-I' that formed several RO$_2$ species at the required RO$_2$ production rate (i.e. k*[A-I] = missing primary production rate, P'(RO$_2$)$_{prim}$). Using the MCM nomenclature (http://mcm.leeds.ac.uk/MCM/home), the RO$_2$ species produced were HOCH2CH2O2, HYPROPO2, IBUTOLBO2, BUTDBO2, OXYBIPERO2, CH3O2 and BUT2OLO2, NBUTOLAO2, and the structures of these RO$_2$ species are shown in Table 6. The RO$_2$ species were chosen after a rate of production analysis (ROPA) analysis showed they were highest produced RO$_2$ species in the model.

The comparison between sum of RO$_2$ observed and sum of RO$_2$ modelled from the model run MCM-P'RO$_2$ demonstrates good agreement in general (Figure 12), although there is a slight overprediction of RO$_2$ in the afternoon and a slight underprediction of RO$_2$ in the morning. However, the MCM-PRO2 run overpredicts the observed HO$_2$ during haze and non-haze events by a factor of 3.4 and 2.5, respectively, with the large overprediction of HO$_2$ in haze and non-haze events driving the overprediction of OH by a factor of 2.2 and 2.5. This highlights that the additional primary RO$_2$ source may be an RO$_2$ species that does not readily propagate to HO$_2$, this has also been discussed in Whalley

660   et al. (2020). To investigate whether the uptake of HO_2 onto the surface of aerosols could improve the agreement between measured and modelled HO_2, the MCM-PRO2 modelled was modified to include the uptake of HO_2 with the uptake coefficient set equal to 0.2, as suggested by Jacob (2000), in model run MCM-PRO2-SA. The measured average aerosol surface area peaked at an average of 6.38×10^{-6} cm^2 cm^{-3}. The comparison of MCM-PRO2-SA with both measurements and MCM-PRO2 (see Table 3

665   for details) shows that the uptake of HO_2 only has a small impact of up to <9% and <6% on the modelled levels of OH, HO_2 and RO_2 during haze and non-haze events, respectively. The aerosol surface area used in the model may be a lower limit as it was calculated from an Scanning Mobility Particle Sizer (SMPS) that only measured aerosols ranging from 10 nm - 1000 nm. At the high levels of NO encountered, the lifetime of HO_2 is short, and the decrease in HO_2 in MCM-PRO2-SA owing to loss

670   onto aerosols is not enough to reconcile measurements with the model and suggests that an additional primary source of RO_2 may not be the cause of the model underprediction of RO_2 species, as the inclusion of additional RO_2 production worsens the model's ability to predict OH and HO_2. If there is missing RO_2 production, the rate of propagation of these species to HO_2 would need to be slower than currently assumed in the model to reconcile the observations of OH, HO_2 and RO_2.

675   The small decrease in modelled HO_2 by heterogeneous uptake contrasts with the recent work from Li et al. (2019) that has shown, using GEOS-Chem, that the observed increasing ozone trend in North China Plain is caused by reduced uptake of HO_2 onto aerosol due to reduction in $PM_{2.5}$ by ~40% between 2013 – 2017.

680

685

690

MCM Name	Structure	MCM Name	Structure
HOCH2CH2O2		BUTDBO2	
HYPROPO2		OXYBIPERO2	
IBUTOLBO2		CH3O2	
BUT2OLO2		NBUTOLAO2	

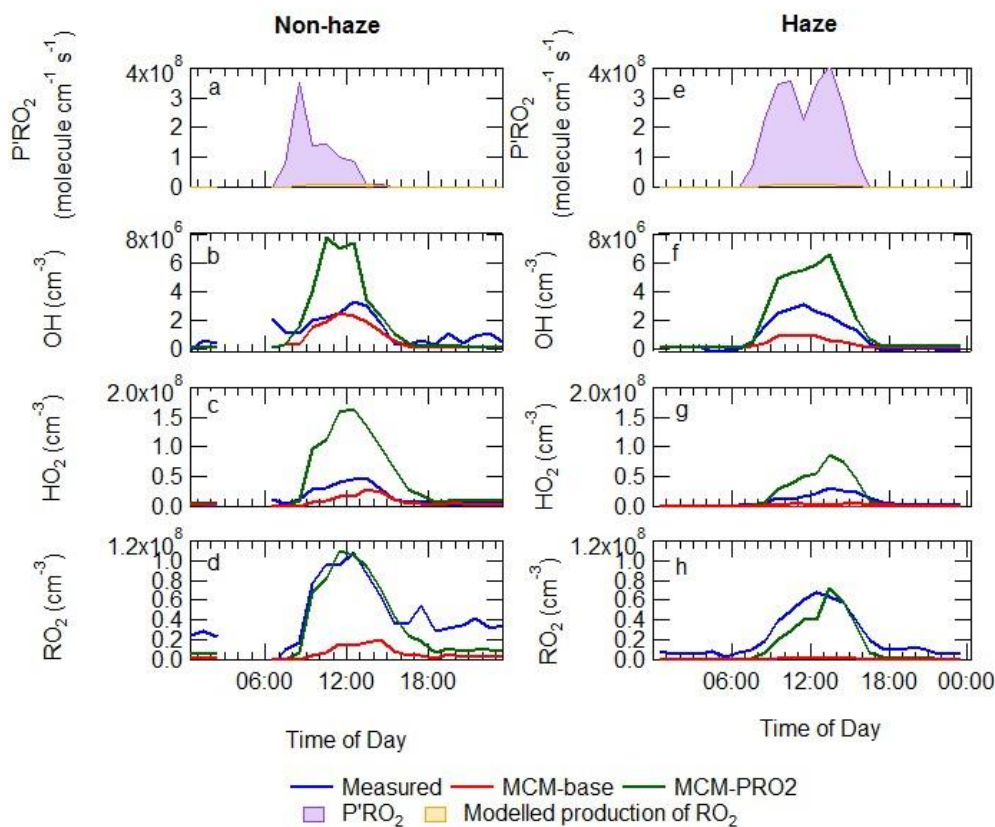**Table 6.** The names and associated structures of the RO_2 species used to add additional primary production of RO_2 species into MCM-PRO2 and MCM-PRO2-SA. See http://mcm.leeds.ac.uk/MCMv3.3.1/home.htt for more details.

Figure 12. Average diel comparison of measurements of P'RO$_2$, OH, HO$_2$ and sum of RO$_2$ with the MCM-base and MCM-PRO2 box-model runs inside (e – h) and outside (a – d) of haze events. The average diel is from the entire APHH winter campaign. See text and Table 3 for definitions of each of the model runs.

4.3 Chemistry of radicals under haze conditions

The observed concentrations of OH during the APHH campaign are much higher than those predicted by global models (~0.4 x 10^5 cm^{-3}, for a 24 hr period average during summertime) in the north China plane (NCP) (Lelieveld et al., 2016), and the OH concentration in and outside of haze events are comparable, despite the lower light levels during these events (on average up to 50% less j(O^{1}D) during the haze events) as shown in Figure 5. The levels of OH are partly sustained during haze events owing to a significant increase in [HONO] in haze (see Figure 5), with HONO being a major source of OH, despite the reduction in *j*(HONO) in haze. The average midday OH reactivity measurements in and out of haze were 47 (s^{-1}) and 17 (s^{-1}), respectively, and since the OH concentrations are comparable in and out of haze, this implies there is a larger turnover rate (defined as the product of [OH] and *k*(OH)), or rate of chemical oxidation initiated by OH radicals, within haze, to balance this. The radical chain length, ChL, is defined by the rate of radical propagation divided by the rate of radical production, and is given by Eq. 4:

$$\mathrm{ChL} = [\mathrm{OH}] \times k_{\mathrm{voc}}/P(RO_x) \qquad\qquad \text{Eq. 4}$$

where k_{VOC} is the total OH reactivity with VOCs and $P(RO_x)$ is the primary production of RO_x radicals. As shown in Table 7 the average of ChL calculated using Eq. 4 during the APHH campaign was ~5.9. This large value indicates that radical propagation during the APHH campaign is very efficient; this ChL is higher than calculated for previous winter campaigns that had OH radical and OH reactivity measurements available, together with VOCs. The large chain length comes from the product of large OH concentrations and high OH reactivity measurements.

Campaign	OH 10^6 cm^{-3}	$P(RO_x)$ (ppbv h^{-1})	kOH (s^{-1})	NO$_2$ (ppbv)	Chainlength ChL	Reference
PUMA, Birmingham	1.7	2.8	30	9.3	2.1	Emmerson et al. (2005) [a]
NY NYC, US	1.4	1.4	27	15	3.3	Ren et al. (2006)
IMPACT Tokyo	1.5	1.4	23	12	3.1	Kanaya et al. (2007) [a]
Boulder	2.7	0.7	5	5	2.0	Kim et al. (2014)
BEST-ONE, Suburban Beijing	2.8	0.9	12	6	4.7	Tan et al. (2017)
APHH, Central Beijing	2.7	1.6	47	30	5.9	This work.

Table 7. Comparison of OH concentration, primary production of RO$_x$ radicals (P(RO$_x$)), OH reactivity (kOH), NO$_2$ concentration and chain length defined by Eqn (4) for various campaigns. The values are a noon-time average. Table modified from Tan et al. (2018). [a] OH reactivity is calculated only.

The average diel profiles of radical concentrations, both measured and calculated by the model, inside and outside of haze periods are presented in Figure 13: the maximum average OH concentration observed is almost the same in and out of haze (~2.7 x 10^6 molecule cm^{-3}) whilst the concentrations of the observed peroxy radicals decrease in haze. The model can replicate OH (within 20%) outside of haze but significantly underpredicts OH inside of haze events. The model also underpredicts HO$_2$ and RO$_2$ during haze, but over-predicts HO$_2$ under the non-haze conditions. The measured complex RO$_2$ radical species peak at similar concentrations inside (4.3 x 10^7 molecule cm^{-3}) and outside (4.6 x 10^7 molecule cm^{-3}) of haze. Interestingly, unlike the complex RO$_2$, the simple RO$_2$ concentration peaks at a lower concentration inside of haze (3.4 x 10^7 molecule cm^{-3}) compared with outside of haze (5.5 x 10^7 molecule cm^{-3}). The complex RO$_2$ is undepredicted by the model by a factor of ~48 and ~12 inside and outside of haze, respectively, whilst the simple RO$_2$ is undepredicted by a factor of ~66 and ~5.7

inside and outside of haze, respectively. The sharp increase for the underprediction of both simple and complex RO_2 inside haze events highlights the need of a large additional primary source of both simple and complex RO_2. The OH reactivity is replicated well by the model both in haze and non-haze conditions. The increased contribution to kOH (s^{-1}) from VOCs going from non-haze to haze conditions is a factor of: ~10 for aromatics, ~8 for alkenes and alkynes , ~6 for alkanes, ~9 for alcohols and ~2 for aldehydes. The large increase in the relative contribution to kOH from aromatics, alkenes and alkynes is consistent with the observation of higher complex RO_2 (compared to simple RO_2) during haze periods compared to non-haze periods. Figure 13 shows the OH concentration observed both in and outside of haze events is significant and indictates that gas-phase oxidation is taking place, and hence the formation of secondary oxidation products, even within haze conditions. Secondary oxidation products, such as nitric acid and sulphuric acid, which partition to the aerosol phase, are major contributors towards the formation of secondary particulate matter (Huang et al., 2014). A discussion on the impact of similar OH concentration inside and outside of haze on the oxidation of SO_2 and NO_2 can be found in the Supplementary Information section S1.3
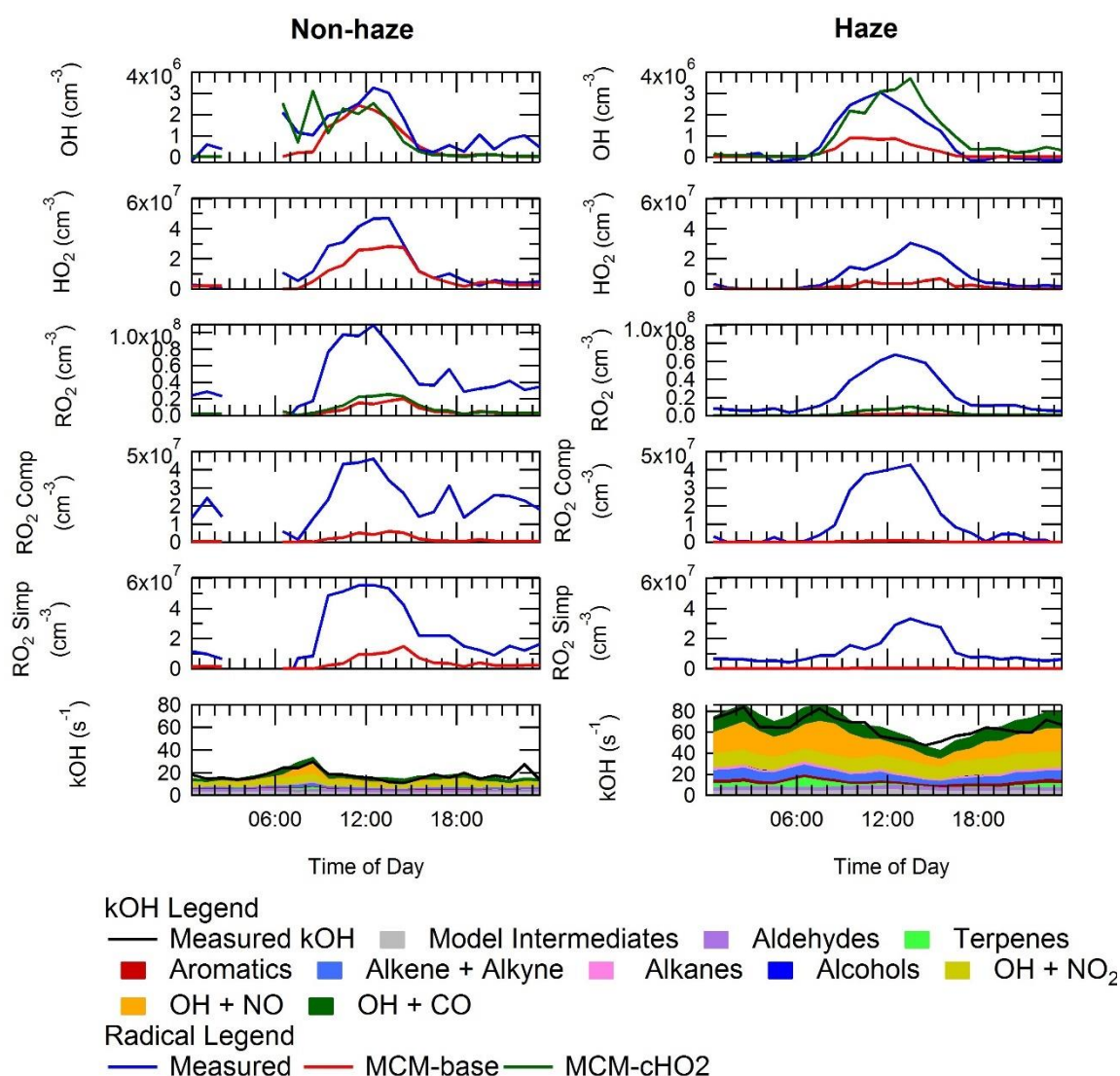
Figure 13. Average diel profiles for measured and modelled OH, HO_2, total RO_2, complex RO_2 (RO_2 comp), simple RO_2 (RO_2 simp) and kOH separated into haze (right) and non-haze (left) periods.

4.4 Implications of model under-prediction of RO_2 radicals on the calculated rate of ozone production

Although ozone pollution is generally not considered a wintertime phenomenon in Beijing, the elevated levels of RO_2 observed under high NO_x conditions suggests that ozone could be produced rapidly, but then is rapidly titrated to NO_2 by reaction with NO. As well as being an important greenhouse gas, O_3 has a negative impact on both human health and crop yields (Lin et al., 2018), and in China led to 74,200 premature deaths and a cost to the economy of 7.6 billion US\$ in 2016 (Maji et al., 2019).

The RO_2 radicals are under-predicted in the model, especially under the higher NO_x conditions, and as shown in Figure 14, this has an implication for the model's ability to predict the rate of *in situ* O_3 production. The rate of O_3 production is assumed to be equal to the net rate of NO_2 production Eq.5:

$$P(O_3) = k_{HO_2+NO}[HO_2][NO] + k_{RO_2+NO}[RO_2][NO] - k_{OH+NO_2+M}[OH][NO_2][M] \qquad \text{Eq. 5}$$
$$- k_{HO_2+O_3}[HO_2][O_3] - P(RONO_2)$$

where RO_2 represents the sum of RO_2, and the last three terms allow for the reduction of ozone production owing to reactions that remove NO_2 or its precursors. The $P(RONO_2)$ term is the net rate of formation of organic nitrate, $RONO_2$, species, for example peroxy acetyl nitrates (PANs).

When the rate of O_3 production is calculated using the measured values of HO_2 and RO_2, there is a positive trend with increasing NO. However, when the modelled concentrations of HO_2 and RO_2 are used, there is a constant $P(O_3)$ across the whole NO range, leading to a large underestimation of O_3 production by the model at higher values of NO. At ~2.5 ppbv and ~177 ppbv of NO the model underestimates the O_3 production by 1.8 and 66, respectively. Figure 14 also shows that there is a high rate of *in situ* ozone production in Beijing in winter and, as shown in Table 8, the maximum rate of ozone production calculated from observed HO_2 and RO_2 is higher for Beijing winter than the corresponding values during the summer-time ClearfLo campaign in London. However, because of the very high NO in Beijing campaign, immediate titration of the O_3 formed results in very low ambient amounts, see Figure 5. As shown in Table 8, the average of the rate of ozone production calculated from observations of HO_2 and RO_2 between 08:00 and 17:00 during our APHH campaign (71 ppbv hr^{-1}, at 40 ppbv of NO) was higher than those calculated using observations during the BEST-ONE campaign (10 ppbv hr^{-1}, at 8 ppbv of NO) and calculated from the measured HO_2 and modelled RO_2 in the PKU campaign (43 ppbv hr^{-1}, at 39 ppbv of NO). An isopleth for ozone showing production as a function of NO_x and VOC for the BEST-ONE campaign (Lu et al., 2019) showed that a reduction in NO_x alone would lead to an increase in O_3 production, and an increase in the amount of secondary organic aerosol produced.
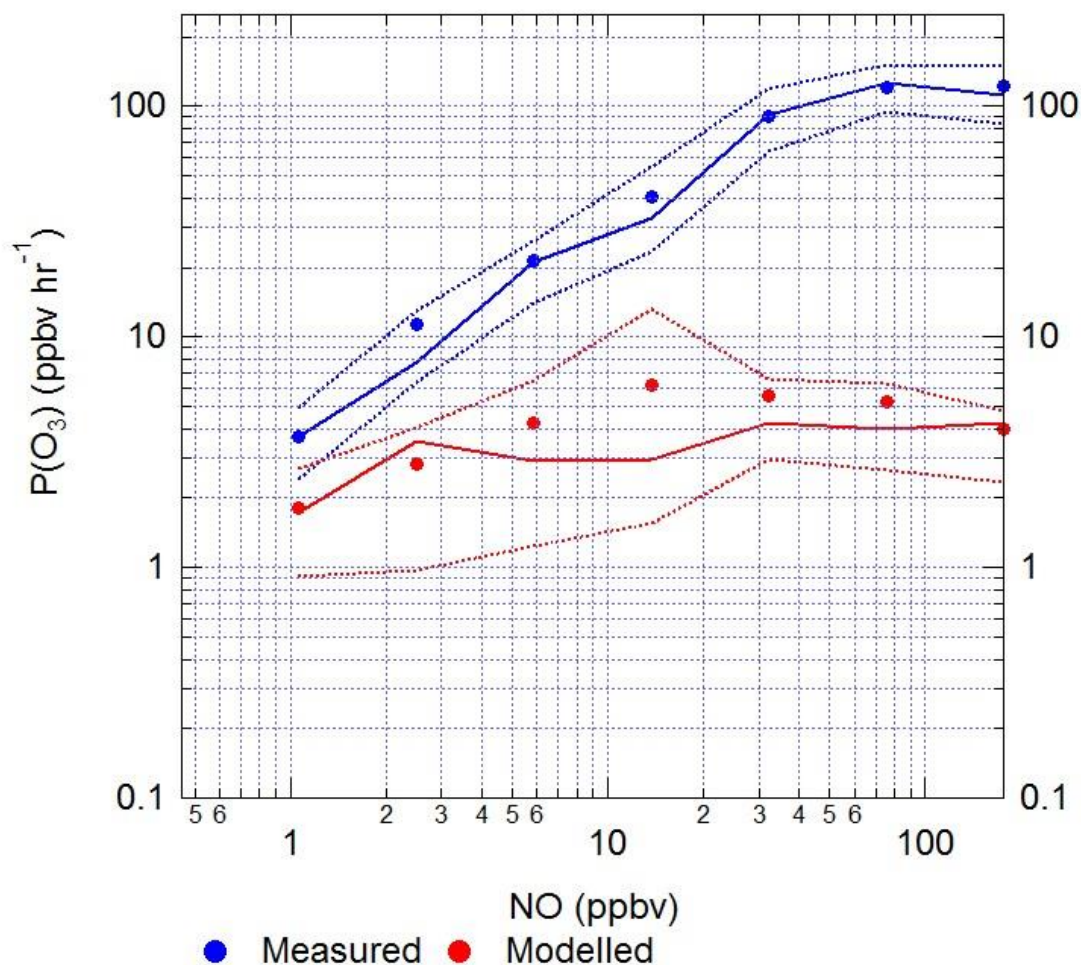
Figure 14. The calculated rate of *in situ* ozone production as a function of [NO] for Eq. 7 using modelled (red) and measured (blue) values of HO_2 and the sum of RO_2 radicals.

The top ten RO_2 species that react with NO to form NO_2 are shown in Figure 15, the top ten RO_2 only contribute to 65.8% of the ozone formed whilst the other 34.2% is from different RO_2's that individually contribute less than 1.5% each. It shows that simple RO_2 species (CH_3O_2 and $C_2H_5O_2$) contribute 26.8% of the total ozone production from RO_2 species.
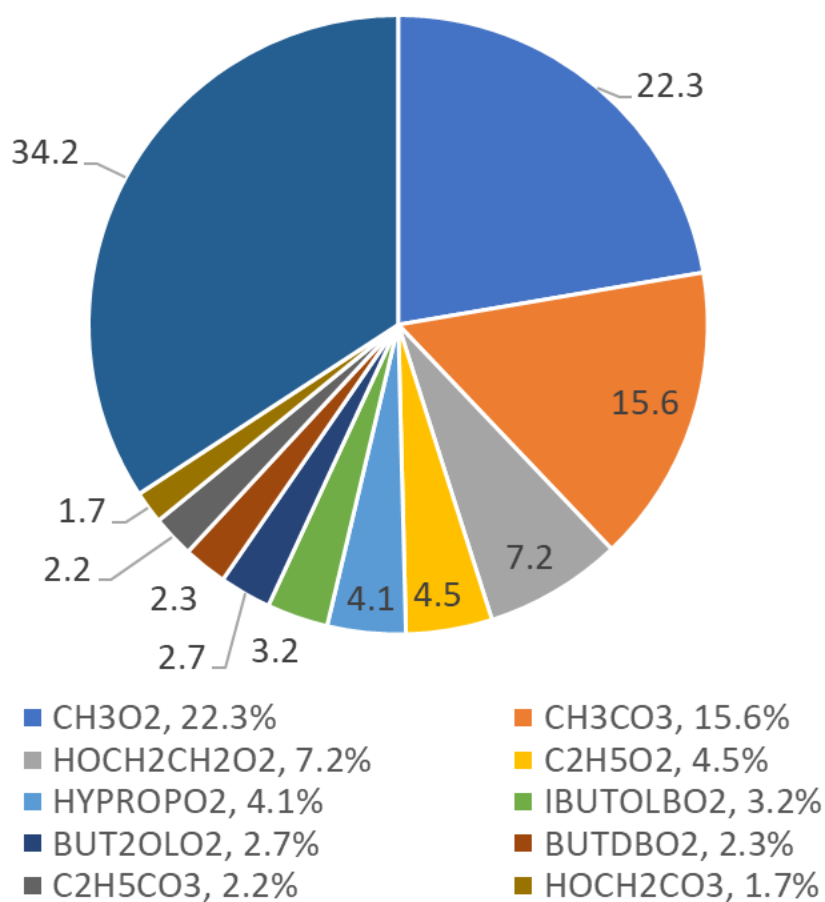
Figure 15. Pie chart showing the top ten RO_2 species that form ozone in the MCM-base model. These top ten RO_2 only contribute to a total of 65.8% of the ozone production, the rest coming from other RO_2 species (34.2%), each with less than a 1.5% contribution to the total production. The names for the RO_2 species are from the MCM, the related structures can be found http://mcm.leeds.ac.uk/MCM/.

Campaign	Dates	NO	P(O$_3$) (ppbv hr^{-1})	Notes	Reference
APHH	Nov – Dec 2016	40	71	Rate average for the daytime periods between 08:00 and 17:00	This work.
		177	123	Maximum ozone production.	
BEST-ONE	Jan – Feb, 2016	8.0	10	Rate average for the daytime periods between 08:00 and 17:00	Tan et al. (2018)
PKU	Nov – Dec 2017	43	39	Rate average for the daytime periods between 08:00 and 17:00	Ma et al. (2019)
ClearfLo	July – Aug 2012	52	41	Maximum ozone production.	Whalley et al. (2018)

Table 8. The rate of *in situ* ozone production averaged between 08:00 – 17:00 for the APHH, BEST-ONE and PKU campaigns and the associated NO concentration. Also shown is the maximum rate of ozone production calculated from measured HO$_2$ and RO$_2$ during the APHH and ClearFLo campaigns.

5. Summary

The APHH campaign took place in central Beijing at the Institute for Atmospheric Physics (IAP) in November and December 2016, with detailed measurements of OH, HO$_2$, sum of RO$_2$ and OH reactivity made using the FAGE technique. High radical concentrations were measured both inside and outside of haze events, despite the lower intensity of solar radiation and therefore photolysis rates in haze. The daily maxima for the radical species varied day-to-day from 1 to 8 x 10^6 cm^{-3}, 0.7 to 1.5 x 10^8 cm^{-3} and 1 to 2.5 x 10^8 cm^{-3} for OH, HO$_2$ and RO$_2$ respectively. Partial speciation of RO$_2$ was achieved, with the sum of simple RO$_2$ deriving from <C$_4$ saturated VOCs reaching a daily maximum concentration between 0.2-1.3 x 10^8 cm^{-3}, and the complex RO$_2$ deriving from larger alkyl, unsaturated and aromatic VOCs reaching a daily maximum concentration between 0.2 and 0.6 x 10^8 cm^{-3}. The partially speciated RO$_2$ measurements showed on average almost 50:50 ratio between the two. The complex RO$_2$ species have higher mixing ratios under high NO (>40 ppbv) conditions whilst simple RO$_2$ have higher mixing ratio at lower NO (<40 ppbv). The average daytime maximum of the radical species was 2.7 x 10^6 cm^{-3}, 0.39 x 10^8 cm^{-3} and 0.88 x 10^8 cm^{-3} for OH, HO$_2$ and total RO$_2$, respectively. The OH radical concentrations are higher than previous winter campaigns outside of China, and comparable to the BEST-ONE campaign that took place in suburban Beijing (60 km northeast of Beijing). The OH reactivity was very high, and showed a significant day to day variability from 10 s^{-1} up to 150 s^{-1} in the most polluted periods. The major contribution to reactivity came from CO (17.3%), NO (24.9%), NO$_2$ (22.1%),

alkanes (3.0%), alkynes and alkenes (10.8%), carbonyls (5.7%), terpenes (3.7%) and model intermediates (6.77%). A steady state calculation for OH showed that the OH budget can be closed using measured HO_2, HONO and k(OH).

The primary production of new radicals by initiation reactions, as opposed to formation via propagation reactions, was dominated (>83%) by the photolysis of HONO, consistent with other winter campaigns. The rate of primary radical production from HONO was observed to increase during haze events, due to the large increase in HONO concentration, even though photolysis rates were considerably lower in haze. Radical termination was dominated by the reaction of OH with NO and NO_2, although under non-haze conditions, when $PM_{2.5} < 75$ μg m^{-3}, the contribution from net-PAN formation became important (~19%).

The comparison of the measurements with a box-model utilising the detailed Master Chemical Mechanism generally showed an underestimation of OH, HO_2 and RO_2. The MCM was able to replicate OH and HO_2 concentrations quite well when [NO] was around 3 ppbv. The model underestimation occurred at [NO] > 2.5 ppbv for OH, HO_2 and RO_2. The underprediction of the radicals reached a measured:modelled ratio of 3, 20 and 91 at 177 ppbv of NO. The under prediction of the peroxy radicals (HO_2 and RO_2) by the model leads to an underestimation of in situ O_3 production under high NO_x conditions. When the MCM is constrained to the measured HO_2, the model can replicate measured OH, and the measured OH reactivity is captured well by the model. This suggests that under high NO_x and haze conditions there is either an additional source of the peroxy radicals or unknown recycling chemistry of RO_2 to HO_2. The OH concentrations inside and outside of haze events were very similar, on average 2.7 x 10^6 molecule cm^{-3}, which suggests that rapid gas-phase oxidation, generating secondary species such as secondary nitrate, sulphate and organic aerosol still occurs in haze events.

References

Ackermann, I. J., Hass, H., Memmesheimer, M., Ebel, A., Binkowski, F. S., and Shankar, U.: Modal aerosol dynamics model for Europe: Development and first applications, Atmospheric environment, 32, 2981-2999, 1998.

Barth, M., Rasch, P., Kiehl, J., Benkovitz, C., and Schwartz, S.: Sulfur chemistry in the National Center for Atmospheric Research Community Climate Model: Description, evaluation, features, and sensitivity to aqueous chemistry, Journal of Geophysical Research: Atmospheres, 105, 1387-1415, 2000.

Chan, C. K. and Yao, X.: Air pollution in mega cities in China, Atmospheric environment, 42, 1-42, 2008.

Cheng, N., Li, Y., Zhang, D., Chen, T., Sun, F., Chen, C., and Meng, F.: Characteristics of ground ozone concentration over Beijing from 2004 to 2015: Trends, transport, and effects of reductions, Atmos. Chem. Phys, 2016. 2016.

Commane, R., Floquet, C., Ingham, T., Stone, D., Evans, M., and Heard, D.: Observations of OH and HO_2 radicals over West Africa, Atmospheric Chemistry and Physics, 10, 8783-8801, 2010.

Crilley, L. R., Karmer, L. J., Ouyang, B., Duan, J., Zhang, W., Tong, S., Ge, M., Ge, K. T., Qin, M., Xie, P., Shaw, M. D., Lewis, A. C., Mehra, A., Bannan, T. J., Worrall, S. D., Priestley, M., Bacak, A., Coe, H., Allan, J., Percival, C. J., Popoola, O. A. M., Jones, R. L., and Bloss, W. J.: Intercomparison of nitrous acid (HONO) measurement techniques in a megacity (Beijing), AMT, 2019. 2019.

Dunmore, R., Hopkins, J., Lidster, R., Lee, J., Evans, M., Rickard, A., Lewis, A., and Hamilton, J.: Diesel-related hydrocarbons can dominate gas phase reactive carbon in megacities, Atmospheric Chemistry and Physics, 15, 9983-9996, 2015.

Ehhalt, D. H. and Rohrer, F.: Dependence of the OH concentration on solar UV, Journal of Geophysical Research: Atmospheres, 105, 3565-3571, 2000.

Emmerson, K., Carslaw, N., and Pilling, M.: Urban atmospheric chemistry during the PUMA campaign 2: Radical budgets for OH, HO 2 and RO 2, Journal of atmospheric chemistry, 52, 165-183, 2005.

Finlayson-Pitts, B., Wingen, L., Sumner, A., Syomin, D., and Ramazan, K.: The heterogeneous hydrolysis of NO 2 in laboratory systems and in outdoor and indoor atmospheres: An integrated mechanism, Physical Chemistry Chemical Physics, 5, 223-242, 2003.

Ge, X., He, Y., Sun, Y., Xu, J., Wang, J., Shen, Y., and Chen, M.: Characteristics and formation mechanisms of fine particulate nitrate in typical urban areas in China, Atmosphere, 8, 62, 2017.

Heard, D. E. and Pilling, M. J.: Measurement of OH and HO2 in the troposphere, Chemical Reviews, 895   103, 5163-5198, 2003.

Hollaway, M., Wild, O., Yang, T., Sun, Y., Xu, W., Xie, C., Whalley, L., Slater, E., Heard, D., and Liu, D.: Photochemical impacts of haze pollution in an urban environment, Atmos. Chem. Phys. Discuss., https://doi. org/10.5194/acp-2019-29, in review, 2019. 2019.

Hopkins, J. R., Jones, C. E., and Lewis, A. C.: A dual channel gas chromatograph for atmospheric analysis 900   of volatile organic compounds including oxygenated and monoterpene compounds, Journal of Environmental Monitoring, 13, 2268-2276, 2011.

Hu, J., Wang, Y., Ying, Q., and Zhang, H.: Spatial and temporal variability of PM2. 5 and PM10 over the North China Plain and the Yangtze River Delta, China, Atmospheric Environment, 95, 598-609, 2014.

Huang, R.-J., Zhang, Y., Bozzetti, C., Ho, K.-F., Cao, J.-J., Han, Y., Daellenbach, K. R., Slowik, J. G., Platt, 905   S. M., and Canonaco, F.: High secondary aerosol contribution to particulate pollution during haze events in China, Nature, 514, 218, 2014.

Jacob, D. J.: Heterogeneous chemistry and tropospheric ozone, Atmospheric Environment, 34, 2131-2159, 2000.

Jenkin, M. E., Valorso, R., Aumont, B., and Rickard, A. R.: Estimation of rate coefficients and branching 910   ratios for reactions of organic peroxy radicals for use in automated mechanism construction, Atmospheric Chemistry and Physics, 19, 7691-7717, 2019.

Kanaya, Y., Cao, R., Akimoto, H., Fukuda, M., Komazaki, Y., Yokouchi, Y., Koike, M., Tanimoto, H., Takegawa, N., and Kondo, Y.: Urban photochemistry in central Tokyo: 1. Observed and modeled OH and HO2 radical concentrations during the winter and summer of 2004, Journal of Geophysical 915   Research: Atmospheres, 112, 2007.

Kim, S., VandenBoer, T. C., Young, C. J., Riedel, T. P., Thornton, J. A., Swarthout, B., Sive, B., Lerner, B., Gilman, J. B., and Warneke, C.: The primary and recycling sources of OH during the NACHTT-2011 campaign: HONO as an important OH primary source in the wintertime, Journal of Geophysical Research: Atmospheres, 119, 6886-6896, 2014.

920   Lang, J., Zhang, Y., Zhou, Y., Cheng, S., Chen, D., Guo, X., Chen, S., Li, X., Xing, X., and Wang, H.: Trends of PM2. 5 and chemical composition in Beijing, 2000–2015, Aerosol Air Qual. Res, 17, 412-425, 2017.

Lee, J., Whalley, L., Heard, D., Stone, D., Dunmore, R., Hamilton, J., Young, D., Allan, J., Laufs, S., and Kleffmann, J.: Detailed budget analysis of HONO in central London reveals a missing daytime source, Atmospheric Chemistry and Physics Discussions, 15, 22097-22139, 2015.

925   Lelieveld, J., Gromov, S., Pozzer, A., and Taraborrelli, D.: Global tropospheric hydroxyl distribution, budget and reactivity, Atmospheric Chemistry and Physics, 16, 12477, 2016.

Li, K., Jacob, D. J., Liao, H., Shen, L., Zhang, Q., and Bates, K. H.: Anthropogenic drivers of 2013–2017 trends in summer surface ozone in China, Proceedings of the National Academy of Sciences, 116, 422-427, 2019.

930   Li, X., Brauers, T., Häseler, R., Bohn, B., Fuchs, H., Hofzumahaus, A., Holland, F., Lou, S., Lu, K., and Rohrer, F.: Exploring the atmospheric chemistry of nitrous acid (HONO) at a rural site in Southern China, Atmospheric Chemistry and Physics, 12, 1497-1513, 2012.

Lin, Y., Jiang, F., Zhao, J., Zhu, G., He, X., Ma, X., Li, S., Sabel, C. E., and Wang, H.: Impacts of O3 on premature mortality and crop yield loss across China, Atmospheric environment, 194, 41-47, 2018.

42

935   Lu, K., Fuchs, H., Hofzumahaus, A., Tan, Z., Wang, H., Zhang, L., Schmitt, S., Rohrer, F., Bohn, B., and Broch, S.: Fast photochemistry in wintertime haze: Consequences for pollution mitigation strategies, Environmental science & technology, 2019. 2019.

Lu, K., Hofzumahaus, A., Holland, F., Bohn, B., Brauers, T., Fuchs, H., Hu, M., Häseler, R., Kita, K., and Kondo, Y.: Missing OH source in a suburban environment near Beijing: observed and modelled OH and

940   HO 2 concentrations in summer 2006, Atmospheric Chemistry and Physics, 13, 1057-1080, 2013.

Lu, X., Wang, Y., Li, J., Shen, L., and Fung, J. C.: Evidence of heterogeneous HONO formation from aerosols and the regional photochemical impact of this HONO source, Environmental Research Letters, 13, 114002, 2018.

Ma, X., Tan, Z., Lu, K., Yang, X., Liu, Y., Li, S., Li, X., Chen, S., Novelli, A., and Cho, C.: Winter

945   photochemistry in Beijing: Observation and model simulation of OH and HO_2 radicals at an urban site, Science of The Total Environment, 685, 85-95, 2019.

Maji, K. J., Ye, W.-F., Arora, M., and Nagendra, S. S.: Ozone pollution in Chinese cities: Assessment of seasonal variation, health effects and economic burden, Environmental pollution, 247, 792-801, 2019.

Mozurkewich, M.: The dissociation constant of ammonium nitrate and its dependence on

950   temperature, relative humidity and particle size, Atmospheric Environment. Part A. General Topics, 27, 261-270, 1993.

Qi, Y., Stern, N., Wu, T., Lu, J., and Green, F.: China's post-coal growth, Nature Geoscience, 9, 564, 2016.

Ren, X., Brune, W. H., Mao, J., Mitchell, M. J., Lesher, R. L., Simpas, J. B., Metcalf, A. R., Schwab, J. J.,

955   Cai, C., and Li, Y.: Behavior of OH and HO2 in the winter atmosphere in New York City, Atmospheric Environment, 40, 252-263, 2006.

Saunders, S. M., Jenkin, M. E., Derwent, R., and Pilling, M.: Protocol for the development of the Master Chemical Mechanism, MCM v3 (Part A): tropospheric degradation of non-aromatic volatile organic compounds, Atmospheric Chemistry and Physics, 3, 161-180, 2003.

960   Shi, Z., Vu, T., Kotthaus, S., Grimmond, S., Harrison, R. M., Yue, S., Zhu, T., Lee, J., Han, Y., and Demuzere, M.: Introduction to Special Issue-In-depth study of air pollution sources and processes within Beijing and its surrounding region (APHH-Beijing), Atmospheric Chemistry and Physics Discussions, 2018. 2018.

Stone, D., Whalley, L. K., and Heard, D. E.: Tropospheric OH and HO_2 radicals: field measurements and

965   model comparisons, Chemical Society Reviews, 41, 6348-6404, 2012.

Stone, D., Whalley, L.K., Ingham, T., Edwards, P., Cryer, D.R., Brumby, C.A., Seakins, P.W. and Heard, D.E., 2016. Measurement of OH reactivity by laser flash photolysis coupled with laser-induced fluorescence spectroscopy. *Atmospheric Measurement Techniques*, pp.2827-2844.

Sun, Y., Wang, Z., Fu, P., Yang, T., Jiang, Q., Dong, H., Li, J., and Jia, J.: Aerosol composition, sources

970   and processes during wintertime in Beijing, China, Atmospheric Chemistry and Physics, 13, 4577-4592, 2013.

Tan, Z., Fuchs, H., Lu, K., Hofzumahaus, A., Bohn, B., Broch, S., Dong, H., Gomm, S., Häseler, R., and He, L.: Radical chemistry at a rural site (Wangdu) in the North China Plain: observation and model calculations of OH, HO 2 and RO 2 radicals, Atmospheric Chemistry and Physics, 17, 663-690, 2017.

975   Tan, Z., Rohrer, F., Lu, K., Ma, X., Bohn, B., Broch, S., Dong, H., Fuchs, H., Gkatzelis, G. I., and Hofzumahaus, A.: Wintertime photochemistry in Beijing: observations of RO x radical concentrations in the North China Plain during the BEST-ONE campaign, Atmospheric Chemistry and Physics, 18, 12391-12411, 2018.

Tang, G., Zhao, P., Wang, Y., Gao, W., Cheng, M., Xin, J., Li, X., and Wang, Y.: Mortality and air pollution in Beijing: The long-term relationship, Atmospheric Environment, 150, 238-243, 2017.

Wang, X., Wang, H., Xue, L., Wang, T., Wang, L., Gu, R., Wang, W., Tham, Y.J., Wang, Z., Yang, L. and Chen, J., 2017. Observations of N_2O_5 and $ClNO_2$ at a polluted urban surface site in North China: High N2O5 uptake coefficients and low ClNO2 product yields. *Atmospheric environment*, *156*, pp.125-134.

Wang, Z., Li, Y., Chen, T., Zhang, D., Sun, F., Wei, Q., Dong, X., Sun, R., Huan, N., and Pan, L.: Ground-level ozone in urban Beijing over a 1-year period: Temporal variations and relationship to atmospheric oxidation, Atmospheric Research, 164, 110-117, 2015.

Whalley, L., Blitz, M., Desservettaz, M., Seakins, P., and Heard, D.: Reporting the sensitivity of laser-induced fluorescence instruments used for HO2 detection to an interference from RO2 radicals and introducing a novel approach that enables HO2 and certain RO2 types to be selectively measured, Atmospheric Measurement Techniques, 6, 3425-3440, 2013.

Whalley, L. K., Stone, D., Dunmore, R., Hamilton, J., Hopkins, J. R., Lee, J. D., Lewis, A. C., Williams, P., Kleffmann, J., and Laufs, S.: Understanding in situ ozone production in the summertime through radical observations and modelling studies during the Clean air for London project (ClearfLo), Atmospheric Chemistry and Physics, 18, 2547-2571, 2018.

Whalley, L.K., Slater, E.J., Woodward-Massey, R., Ye, C., Lee, J. D., Squires, F., Hopkins, J. R., Dunmore, R. E., Shaw, M., Hamilton, J. F., Lewis, A. C., Mehra, A., Worrall, S. D., Bacak, A., Bannan, T. J., Coe, H., Ouyang, B., Jones, R. L., Crilley, L. R., Kramer, L. J., Bloss, W. J., Vu, T., Kotthaus, S., Grimmon, S., Sun, Y., Xu, Weiqi., Yue, S., Ren, L., Acton, W. J. F., Hewitt, C. N., Wang, X., Fu, P. and Heard, D. E : Evaluating the sensitivity of radical chemistry and ozone formation to ambient VOCs and NOx in Beijing, *Atmos. Chem. Phys Disc*, 2020

Whalley, L. K., Stone, D., Dunmore, R., Hamilton, J., Hopkins, J. R., Lee, J. D., Lewis, A. C., Williams, P., Kleffmann, J., and Laufs, S.: Understanding in situ ozone production in the summertime through radical observations and modelling studies during the Clean air for London project (ClearfLo), Atmospheric Chemistry and Physics, 18, 2547-2571, 2018.

Woodward-Massey, R., Slater, E. J., Alen, J., Ingham, T., Cryer, D. R., Stimpson, L. M., Ye, C., Seakins, P. W., Whalley, L. K., and Heard, D. E.: Implementation of a chemical background method for atmospheric OH measurements by laser-induced fluorescence: characterisation and observations from the UK and China, Atmos. Meas. Tech., 13, 3119–3146, https://doi.org/10.5194/amt-13-3119-2020, 2020.

Zaveri, R. A., Easter, R. C., Fast, J. D., and Peters, L. K.: Model for simulating aerosol interactions and chemistry (MOSAIC), Journal of Geophysical Research: Atmospheres, 113, 2008.

Zhang, H., Wang, S., Hao, J., Wang, X., Wang, S., Chai, F., and Li, M.: Air pollution and control action in Beijing, Journal of Cleaner Production, 112, 1519-1527, 2016a.

Zhang, L., Wang, T., Zhang, Q., Zheng, J., Xu, Z., and Lv, M.: Potential sources of nitrous acid (HONO) and their impacts on ozone: A WRF-Chem study in a polluted subtropical region, Journal of Geophysical Research: Atmospheres, 121, 3645-3662, 2016b.

Zhou, X., Gao, H., He, Y., Huang, G., Bertman, S. B., Civerolo, K., and Schwab, J.: Nitric acid photolysis on surfaces in low-NOx environments: Significant atmospheric implications, Geophysical Research Letters, 30, 2003.